DEACTIVATION AND SPINEL PHASE REGENERATION OF REDUCED NICKEL ALUMINATE

BY

ALEC C. LADONIS

A THESIS

SUBMITTED TO THE FACULTY OF

ALFRED UNIVERSITY

IN PARTIAL FULFILLMENT OF THE REQUIREMENTS

FOR THE DEGREE OF

MASTER OF SCIENCE

IN

MATERIALS SCIENCE AND ENGINEERING

ALFRED, NEW YORK

SEPTEMBER, 2016

DEACTIVATION AND SPINEL PHASE REGENERATION OF REDUCED NICKEL ALUMINATE

BY

ALEC C. LADONIS

B.S. ALFRED UNIVERSITY (2014)

SIGNATURE OF AUTHOR _____

APPROVED BY _____
SCOTT T. MISTURE, ADVISOR

_____
ERIC J. PAYTON, CO-ADVISOR

_____
STEVEN M. PILGRIM, ADVISORY COMMITTEE

_____
DAVID W. LIPKE, ADVISORY COMMITTEE

_____
CHAIR, ORAL THESIS DEFENSE

ACCEPTED BY _____
ALASTAIR N. CORMACK, INTERIM DEAN
KAZUO INAMORI SCHOOL OF ENGINEERING

Alfred University theses are copyright protected and may be used for education or personal research only. Reproduction or distribution in part or whole is prohibited without written permission from the author.

Signature page may be viewed at Scholes Library, New York State College of Ceramics, Alfred University, Alfred, New York.

ACKNOWLEDGMENTS

First, I must thank my parents, David and Carla Ladonis, who instilled values such as hard work, persistence, and education in me as a young student. Without their support throughout my academic career, I could not have achieved my full potential. Second, I must thank my little brothers, Zachary and Joshua for keeping my focus on work.

Next, I must thank my friends and colleagues at Alfred University, past and present. Being a part of this community, academically and socially, has been a privilege that I would like to continue. I must single out Yuri Coutinho, Wendy Tan, Peter Sowinski, Corine Pettit, Rob Locker, and Nick Cantafio. All have provided particulars with instrumentation or programming, have shown me how to think critically about and present research, and have had thought provoking conversations. I would also like to thank previous graduates Brendan Hill, Michelene Hall, Kate Glass, and Kyle McDevitt for their impeccable job at preserving and organizing their data for future use.

A much needed thanks goes out to the technical specialists at Alfred, particularly Swavek Zdzieszynski and Gerry Wynick. Without your hard work and expertise, instruments used in this during my thesis would not be in working condition. Thank you for an unimpeachable job, as well as your teaching, analysis and guidance.

I also want to thank my committee members, Steven Pilgrim and David Lipke, whose questions fostered a much better final product than I would have produced without them.

Special thanks to Dr. Jane Howe for her expertise in performing measurements outside Alfred University, as well as thoughtful conversations that led to a better understanding of the material. Acknowledgements for the use of the Hitachi LV-SEM follow: This research was supported in part by Oak Ridge National Laboratory's SHaRE User Facility, which is sponsored by the Scientific User Facilities Division, Office of Basic Energy Sciences, U.S. Department of Energy. Part of this research was conducted at the Center for Nanophase Materials Sciences, which is sponsored at Oak Ridge National Laboratory by the Division of Scientific User Facilities, U.S. Department of Energy.

Other special thanks go to Eric Payton, for his guidance at both Alfred University and at the Air Force Research Lab in Dayton, serving on my committee as a co-advisor. Without your constant communication and support, this work would not be possible.

Finally I want to thank my advisor, Scott Misture. He encouraged me to push my limits, think critically, and learn to achieve a deeper understanding. I was allowed me great freedom in determining the direction of my project which made the results personally gratifying. Under his guidance, I've grown to appreciate the art of research.

Alfred has been a great home to me for the past six years. Nearly all my friends have some connection to our little community, and I am grateful to be a part of it.

TABLE OF CONTENTS

Page

LIST OF TABLES

Page

LIST OF FIGURES

Page

ABSTRACT

Nickel aluminate ($NiAl_2O_4$) is an attractive material for dry reforming of methane due to selective reduction yielding catalytically active Ni metal particles. However, during this process, the catalyst is subject to mechanisms that ultimately degrade the catalytic activity. In the present work, characterization of reduced $NiAl_2O_4$ + 2.5 wt. % ZrO_2 (Ni + defect spinel) via novel *in-situ* low voltage high resolution high temperature scanning electron microscopy (HTSEM) coupled with *in-situ* high temperature X-ray diffraction (HTXRD) is investigated to address:

1. The feasibility of observing surface behavior during deactivation and regeneration of the catalyst by reduction and reoxidation;
2. Surface and bulk microstructural evolution during thermal exposure; and
3. Stability of surface and bulk morphology over time at operating temperatures.

This work reveals surface microstructural and topographical features as well as their effects on functional behavior that can be observed via *in-situ* HTSEM. However, challenges in the analysis include local control of pO_2, damage to the specimen surface, and the inability to replicate exact service conditions in terms of flowing gasses.

HTXRD performed in air demonstrates that oxidation of Ni occurs between 400-500°C, and concludes by 900°C. Spinel XRD peaks grow upon oxidation, indicating phase regeneration. HTXRD under industrial grade N_2 with small amounts of oxygen exhibit spinel, Ni metal, and ZrO_2 peaks until 1100°C is reached, no NiO formation is exhibited, even upon cooling. An increase in spinel peak intensity is also observed under N_2 with 5-20 ppm pO_2.

HTSEM demonstrates that Ni metal surface particles migrate and coalesce upon the support surface between 900-1000°C revealing pit structures upon the surface. The composition of the primary particles is unknown due to differences in pO_2 between HTSEM and HTXRD, but is expected to be Ni metal. Mechanisms for particle movement are also unclear; movement is not gravity driven and Ni is a solid at this temperature. Additional reduction of the matrix is observed between 900-1000°C, which is likely due to low pO_2 within the SEM chamber. Above 1000°C, all observed particles reincorporate into the matrix, exposing pit like structures on the surface, similar to ones observed post migration. These pits do not heal with time at temperature; instead the pits and crevices mature with time as evidenced by sharpening of edges and corners of crystalline facets. The overall reduction and reoxidation process is expressed as:

$$NiAl_2O_4 \xrightarrow{H_2+heat} Ni_{1-x}Al_2O_{4-x} + xNi + \frac{x}{2}O_2 \xrightarrow{O_2+heat} xNiO + Ni_{1-x}Al_2O_{4-x} \xrightarrow{time+heat} NiAl_2O_4.$$

HTSEM provides direct evidence that particles migrate and coalesce during the initial steps of catalyst regeneration, revealing a roughened surface with pits and crevasses. This surface rearrangement may provide longer distances for particle migration to occur, slowing the coalescence and regeneration of the original spinel to improve the catalyst service time.

I. INTRODUCTION

A. Importance

Compounds with the spinel structure are commonly the focus of study for electrical, magnetic, and high temperature investigations, derived directly from the chemical flexibility of the structure. Spinel has become the model system to study tetrahedral vs. octahedral coordination for differing ions.[1] Nickel aluminate ($NiAl_2O_4$) has been identified as a spinel of high technological importance attributable to its advantageous properties which include high thermal stability and high temperature reduction characteristics for catalytic purposes for applications such as an anode in Al production. The reducibility at elevated temperatures creates an oxide supported Ni metal composite with beneficial catalytic properties for wet and dry reforming of methane to produce H_2. However, deactivation of the Ni occurs by particle sintering, oxidation, and contamination at operation temperatures during reforming. It is known that Ni particles can be reabsorbed into the remnant oxide support and subsequently reduced, removing the contaminants and regenerating the composite. Characterization has been previously conducted by our group as well as others to better understand these deactivation and regeneration mechanisms,[2–12] but little investigation has been conducted outside of transmission electron microscopy (TEM) and X-ray photoelectron spectroscopy due to the submicron features. With major advances in materials characterization technology - specifically low accelerating voltage SEM imaging, *in-situ* high temperature furnaces and fast high resolution detectors - new insights may be possible into hypothesized deactivation and regeneration mechanism(s).

B. Crystal Structure

Spinel normally takes the general chemical formula of AB_2X_4, and is regarded as a simple structure type. This is an oversimplification; the crystal structure is quite complex. Structural rearrangement allows for non-stoichiometry and cation substitution. In the chemical formula, A and B cations are normally +2 and +3 elements in the valence state which reside on the tetrahedral and octahedral sites, respectively. The anion, X, is

normally oxygen, but can be a chalcogenide anion such as sulfur, selenium, or tellurium.[13] Figure 1 shows a perspective of the unit cell along the [100] axis as well as a tilted view. The Bravais lattice for the spinel family is face centered cubic (FCC), consisting of 8 formula units per unit cell resulting in 32 anions and 24 cations. Space group designation for the structure is Fd$\bar{3}$m, International Tables for crystal number 227. Out of the 64 tetrahedral and 32 octahedral interstices only 8 tetrahedral and 16 octahedral interstices are occupied. Two choices are present for the origin of the space group, $\bar{4}3m$ and $\bar{3}m$. For this work, the latter will be used.

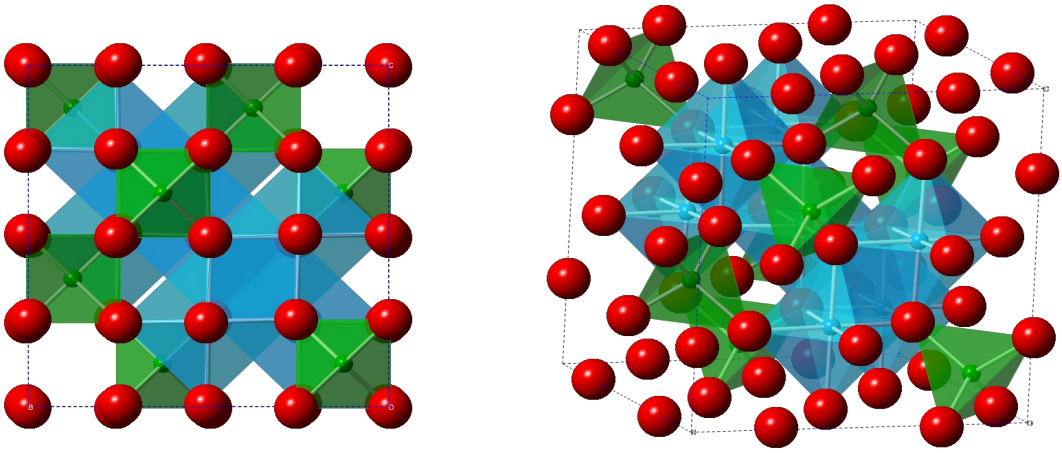

Figure 1: Unit cell of a general spinel. Left: [100] perspective, Right: tilted perspective. Red atoms represent oxygen while blue and green represent cations. Colors emphasize octahedral (blue) vs. tetrahedral (green) coordination.

For an origin on the $\bar{3}m$ location, the tetrahedral site and octahedral site are special positions, located at x = 0.125, y = 0.125, and z = 0.125 (Wycoff position 8a), and x = 0.5, y = 0.5, z = 0.5 (Wyckoff position 16d) respectively.[14] Anion arrangement is cubic close packing along the [111], although deviations are present depending on spinel composition. To describe variations among all spinel types accounting for the wide array of compositions, three degrees of freedom have been defined: the lattice parameter, *a*, the inversion parameter, *i*, and the anion (oxygen in this case) parameter, *u*.[14]

Lattice parameters of spinel are large, *a* = 8.083 Å for $MgAl_2O_4$ and *a* = 8.045-8.048 Å for $NiAl_2O_4$.[1, 15] Inversion parameter, *i*, refers to the occupancy of the B site cations located on the tetrahedral sites; mathematically, the fraction of B cations

occupying the tetrahedral sites divided by the total amount of tetrahedral sites. Classifications denote the type of spinel; normal, random and inverse have corresponding values of $i = 0$, $i = 0.66$, $i = 1$. In a normal spinel, A cations occupy all the tetrahedral sites and some octahedral sites, while B cations occupy the octahedral sites, resulting in $i = 0$. Random spinel occurs when a two thirds of the B cations occupy the tetrahedral sites ($i = 0.66$). A fully inverse spinel consists of all the tetrahedral sites being occupied by the B cation, with the octahedral sites shared equally between the A and B cations. Spinel vary in inversion parameter depending on composition, temperature, ionic charge, ionic radius, and anion polarization.[1, 16, 17]

Oxygen parameter, u, has typical values ranging from $u = 0.240$ to 0.275, with a value of $u = 0.25$ for perfect cubic close packing along the [111] for $\bar{3}m$ symmetry derived from the octahedral and tetrahedral bond lengths.[15, 17, 18] As the value increases from $u = 0.25$, oxygen ions shift along the [111], creating an expansion of the tetrahedral site and concurrent shrinkage of the octahedral site. O'Neill and Navrotsky[17] expressed the bond lengths of cation to anion distances, where R is the distance from cation to anion by Equations 1 and 2:

$$\boldsymbol{R_{tet} = a\sqrt{3\left[u - \frac{1}{8}\right]}} \quad (1)$$

$$\boldsymbol{R_{oct} = a\sqrt{3u^2 - 2u + \frac{3}{8}}}\,. \quad (2)$$

Sickafus et al. has compiled data throughout the literature on spinel and mathematically connects composition to the lattice parameter and oxygen parameter, based upon average atomic radii of the cations.[14] This can be used to calculate the theoretical bond lengths (Equations 1 and 2), where compositional variations significantly affect the structure and therefore material properties, e.g. the preferred diffusion modes.

C. $NiAl_2O_4$ Structural Parameters

Structural parameters are compiled in Table I for $NiAl_2O_4$ spinel and a common $MgAl_2O_4$ spinel for reference. As shown, the Ni spinel has a much higher density and

slightly larger lattice, attributable to Ni^{2+} having a larger atomic mass and radius compared to Mg^{2+}. One significant difference of note is the inversion parameter, with the Mg spinel being relatively normal and the Ni spinel highly inverse. The variation in lattice parameter of the Ni spinel stems from the long equilibration time for the cation distribution at low temperatures.

Table I: Structural Parameters for $NiAl_2O_4$ and $MgAl_2O_4$

	$\rho\ \left[{}^{g}/_{cm^3}\right]$ [19]	Lattice Parameter (a) [Å][1, 15]	Oxygen Parameter (u)[15, 18]	Inversion Parameter (i)[18, 20]
$MgAl_2O_4$	3.58	8.083	0.2624	0.05-0.33
$NiAl_2O_4$	4.5	8.045-8.048	0.254-.0256	0.86-0.9

D. Spinel Reduction

$NiAl_2O_4$ reduction studies are plentiful in the literature,[21–26] mainly for catalytic and structural applications. It is known that Ni^{2+} is extracted from the spinel under sufficiently low oxygen partial pressures (pO_2) at high temperatures, with corresponding extraction of O^{2-} from the structure. In previous work performed at Alfred University, it has been shown that extraction of Ni^{2+} and O^{2-} from the spinel creates both V_{Ni}'' and $V_O^{\cdot\cdot}$, which remain within the structure until the temperature is increased above 1000°C, where metastable alumina is formed.[12, 27, 28] Loss of oxygen upon reduction of spinel is also supported by works of Okuyama et al. and Quénard et al.[29, 30] It is also clear that the vacancies created upon reduction do not accumulate, but rather diffuse in a codependent manner to the surface or to internal porous structures with ions to maintain local charge neutrality. Equation 3 describes Ni removal from a spinel of $Ni_xMg_{1-x}Al_2O_4$, resulting in an Mg and Al rich spinel where the vacancies have been included to demonstrate their production.[11, 31]

$$xH_2 + Ni_xMg_{1-x}Al_2O_4 \rightarrow xNi + Mg_{(1-x)\left(\frac{4}{4-x}\right)}Al_{2\left(\frac{4}{4-x}\right)}O_{4-x} + xV_{Ni}'' + xV_O^{\cdot\cdot} + xH_2O \quad (3)$$

Equilibrium phase diagrams for the Ni-NiO and the ($NiAl_2O_4$ + NiO) – ($NiAl_2O_4$ + Ni) systems have been determined by Elrefaie and Smeltzer between 850 and 1150°C.[32] From EMF measurements, a coexistence between Ni, NiO and $NiAl_2O_4$

occurs at 1000°C when the $pO_2 = 3.76 \cdot 10^{-11}$ atm, which is slightly different than the estimated Ni-NiO equilibrium $pO_2 = 4.48 \cdot 10^{-11}$ atm at the same temperature via the Ellingham diagram.[33] A Ni-Al alloy was found to exist under a $pO_2 \approx 10^{-23}$ atm. However, later studies of the Ni-NiO system have shown that the small variance between equilibrium pO_2 of Ni-NiO and $NiAl_2O_4 + NiO$ – -> $NiAl_2O_4 + Ni$ is much larger than originally anticipated by Elrefaie and Smeltzer's EMF values. Taylor and Dinsdale demonstrate through magnetic properties and a "compound-energy" model that equilibrium between Ni and NiO occurs at a temperature of 1055°C at a $pO_2 = 2 \cdot 10^{-10}$ atm which is also supported by the works of Mermelstein et al. as well as Kowalski and Spencer and the general Ellingham diagram by Kishimoto et al.[33–36]

Reduction in a closed system has factors that limit the extent of reduction that a sample can undergo. Sample mass, system volume, and moisture content all play integral roles in determining the microstructure produced upon reduction. At the start of the reduction process, X and Y moles of H_2 and H_2O are present within the system, respectively. Considering that the chamber is continuously being evacuated while heating and that H_2 is being pumped into the system once the predetermined temperature is reached, moles of H_2O should be small compared to those of H_2. This can be used to determine the pO_2 of the system as a function of temperature using:

$$2H_2(g) + O_2(g) \leftrightharpoons 2H_2O(g) \tag{4}$$

$$\Delta G^{\circ} = -RTln(K_p) \tag{5}$$

$$K_p = \frac{(p_{H_2O})^2}{(p_{H_2})^2 (p_{O_2})} \tag{6}$$

$$pO_2 = e^{\frac{-\Delta G^{\circ}}{RT}} \left[\frac{(p_{H_2})^2}{(p_{H_2O})^2} \right] \tag{7}$$

$$H_2 + Ni_{Ni}^0 + O_O^0 \rightarrow H_2O + Ni^0 + V_{Ni}^{''} + V_O^{\cdot\cdot} \tag{8}$$

Equation 8 will progress forward as long as the oxygen pressure is less than the dissociation pressure consuming H_2 to produce H_2O. Equation 4 will shift to establish equilibrium, essentially reversing the reaction to increase the pO_2 of the system. This

slows the overall reduction, along with the build-up of a reaction layer upon the surface of the spinel, increasing the diffusion distance and slowing the reaction rate. The reaction rate will continue to decrease until equilibrium is reached between the phases present. In theory, X moles of H_2 can reduce X moles of Ni from the spinel, as long as the pO_2 is kept below the dissociation pressure of the spinel and the reducible moles of Ni are equal to the number of moles of H_2, all of which depend on sample mass, furnace volume and pressure.

Under flowing reduction conditions, the reacted feed gas is swept away from the sample and thus the pO_2 will remain constant for any specific temperature. Equation 8 is thus true for flowing reduction, but the rate at which the reaction occurs is time dependent based upon diffusion within the samples. Larger distances (and therefore reaction times) prolong the diffusion of the oxygen and nickel ions to the surface.

The extraction of the Ni^{2+} and the O^{2-} from the structure leaves behind a defective non-stoichiometric spinel phase that is rich in Mg and Al for the previous solid solution case. If one assumes that the Ni content approaches X = 1, then the spinel can be described as an alumina rich spinel which has an oxygen sublattice and cation vacancies similar to γ-alumina.[10, 37, 38] This directly relates the reduction of the remnant spinel to the γ-alumina structure.

E. Transition Alumina and ZrO_2 Additions

It is known that alumina has many different metastable polymorphs which differ greatly in surface area to support metallic catalysts. These thermodynamically metastable phases can be categorized into two groups based on the arrangement of the oxygen sublattices. Gamma (γ) alumina falls into the category of a defect spinel structure (FCC oxygen sublattice), while θ-alumina falls into a monoclinic crystal lattice with a space group of $C2/m$. Corundum or α-alumina can be categorized as a rhombohedral crystal lattice with a space group of $R\bar{3}c$. It has been proven that the γ-alumina structure undergoes transitions to a mixed (γ + θ) phase at 900°C, then to a mixed (θ + α) phase at 1100°C, and finally to corundum (α-alumina) at 1300°C, with decreasing surface area throughout the transition sequence, lowering the locations for Ni particles.[26, 37] The

corundum phase has a significant reduction in surface area compared to the transition alumina polymorphs; 194 m^2/g for γ-alumina to 4 m^2/g for α-alumina which was determined by Chary et al. through BET measurements.[26] Therefore, low surface area θ-alumina and corundum are not an ideal supports for catalytic metal particles which also lack the close packed oxygen sublattice for regeneration.

To combat this transition to α-alumina and maintain a reversible remnant oxide during regeneration, matrix modifiers have been used with moderate success. The most effective additive in retarding the transition of γ → α-alumina is ZrO_2. Previous work shows that small additions of ZrO_2 and Nb_2O_5 reduce the development of metastable spinel compared to undoped $NiAl_2O_4$, whereas TiO_2 additions accelerate the formation of corundum under the same experimental conditions.[28] The effects of adding ZrO_2 to the alumina matrix are described by Üstündag et al. who found that small additions (no more than 2.5%) of ZrO_2 can prevent grain boundary cracking and inhibit spinel grain growth, 50-100 μm grains compared to 2 μm for undoped and doped samples respectively.[39] This group also has demonstrated that ZrO_2 additions increase the kinetics of reduction, with doped samples exhibiting a reaction layer of 100-170 μm in comparision to 12-13 μm for the undoped samples.[39] This work is also supported by Han et al. who tested a series of mesoporous Ni-Al_2O_3-ZrO_2 xerogel catalysts with varying Zr/Al molar ratios.[40] An assessment of the stability of the series $Ni_XMg_{1-X}Al_2O_4$ + 2.5 wt. % ZrO_2 with respect to composition and reduction temperature demonstrated that at a composition of X = 1 and temperatures above 900°C, the remnant spinel transitions to a θ-alumina polymorph, making the remnant spinel unstable.[28]

F. Nickel Crystallite Shape

The extraction of the nickel from the spinel via reduction with H_2 creates Ni metal crystallites on the surface of the now defect spinel. The effects on catalytic activity of crystallite shape, size, and location to the support surface can be measured by turnover frequency (TOF). TOF is defined as revolutions of the catalytic cycle per unit time, normally seconds.[41] It has been reported that catalysts tested in this study at 850°C have a TOF of 3.9 [s^{-1}], which is obtained for methane reforming.[12] In comparison, at 550°C, Ni

catalysts supported by α-Al_2O_3 and ZrO_2 show TOFs ranging from 1.7-3.7 [s^{-1}].[42] Pt catalysts TOF values are normally < 2[s^{-1}] at 550°C on the same α-Al_2O_3 and ZrO_2 as a reference from the same study.[42]

Nickel crystallizes in an FCC arrangement, low index planes of the {111} and the {100} variety are the most energetically favorable due to surface energy minimization.[43–48] These studies consist of variations on the Embedded Atom Model (EAM), but the Meltzman paper[47] is of experimental significance. A nickel film was deposited upon the surface of sapphire under H_2 and thus exploited the wetting conditions of the nickel metal at 1300°C and 1350°C to investigate particle shape. Using a Wulff shape simulation, i.e. simulating the equilibrium shape according to the Gibbs thermodynamic principle, the researchers were able to identify low index planes of the {111} and the {100} type consistent with EAM simulations.[43–48]

G. Nucleation, Growth, and Diffusion

The final microstructure is dependent on particle or grain size, composition, and temperature associated with the reduction. Small particles/grains yield more rapid Ni reduction based upon higher surface areas which produce more nucleation sites, as well as shorter distances for diffusion to occur along grain boundaries. Since the slowest diffusion is lattice or bulk diffusion, faster diffusion routes such as grain boundary, surface, and "short circuit" diffusion along crystallographic imperfections will influence the internal microstructure.

Equation 4 requires H_2 gas for the reaction to progress, which in turn suggests that the Ni^{2+}, O^{2-}, and H_2 or similar species must be brought together to form H_2O. It is not known whether H_2, OH^-, H^+, or a combination of species diffuse through the bulk. Near the surface of the particle, diffusion by bulk, grain boundaries and short circuit mechanisms occur,[39, 49] which allows for an oxygen depleted region around the particle surface. Reduction of the bulk most likely occurs by short circuit diffusion, but the extent of this cannot be determined due to microstructural and reduction temperature variations.[49]

It is also known that temperature and the oxygen partial pressure affect Ni particle location and size upon the support.[28] Temperature affects the plethora of the Ni crystallites, which decrease in abundance but increase in size, presumably by an Ostwald ripening or a surface diffusion mechanism. Particles seem to be highly ordered upon the surface, but no explanation has been presented within the literature.

H. Catalyst Regeneration

Regeneration is the process of making the catalyst reusable after accumulation of carbon and/or sulfur poisoning from reactions with the process gas has occurred. The accumulation of contaminants on the surface slowly reduces the catalytic activity until full deactivation occurs. Catalyst regeneration enables extended use of the same material by the partial removal of contaminants deposited upon the surface resulting in slight losses in catalytic activity. Typical losses associated with regeneration are based upon effectiveness of contaminant removal and dispersion of the active metal phase on the support upon reduction. Regeneration processes differ greatly throughout the literature depending on structure and composition.[11, 50–54]

Regenerable catalysts begin with an oxide host that can be reduced to a remnant oxide supported metal composite. This was pioneered by Tanaka in the 2000's, for Pt, Pd, and Rh supported on perovskite structures for automotive catalysts.[55] Upon reduction, metal is extracted from the matrix, leaving metallic nanoparticles supported by a remnant oxide. These metallic particles are subject to the deactivation mechanisms explained earlier, but can be regenerated by the reincorporation of the metal back into the remnant oxide, recreating the original or "parent" phase and removing the contaminants via oxidation. This process of "thermal impregnation" has also been developed for glassy oxide supports by Felix and coworkers.[56–60]

Regeneration is only possible if the catalyst has a remnant oxide structure or a structure that can be converted back into the original parent phase under oxidizing conditions. Transition alumina, specifically γ-alumina, provides a close packed oxygen sublattice with vacancies that provide a foundation to rebuild the spinel upon oxidation. Previous work in our group has shown that for temperatures below 1000°C, the

oxidation/regeneration processes are completely reversible for Ni, Ni-Mg, Ni-Co and Ni-Mg-Co spinel catalysts.[12] Below this temperature, the formation of the transition alumina is minimized and corundum is not formed. The microstructure of the spinel remains intact, indicating that the phase assemblages are also intact. It is important to note that the Ni goes through an oxidation process to NiO, and then transitions back into the remnant spinel at higher temperatures to recover the initial spinel composition.[10]

I. High Temperature Scanning Electron Microscopy

High temperature scanning electron microscopy (HTSEM) and TEM have been utilized as analytical methods since the mid 1990's and have a multitude of applications.[61–63] These include corrosion and oxidation of metals, sintering, high temperature reactivity, hydrogen desorption, reduction oxidation reactions, magnetic properties, microstructural evolutions and modifications, thermal decomposition, and self-healing/self-repairing materials. An extensive list of references for these applications can be found in Podor's book chapter of *Scanning Electron Microscopy*.[64]

HTSEM is an excellent tool for the continuous *in-situ* observation of temperature effects on a specific material in either vacuum or in a controlled atmosphere such as H_2O, He + H_2, N_2, air, etc.[64–66] A specific drawback to this technique is the decrease in resolution of images at high temperature due to thermal electron emission, flooding the Faraday Cage on the secondary electron detector. Another downfall to the technique is outgassing of the sample and chamber/pump integrity upon heating. Heated gasses are ionizable and tend to give off electrons when the beam interacts with the gas. Some samples when heated may give off volatiles that are harmful to the SEM system, mainly the gun, chamber, detector, vacuum, and pump systems that shorten the lifespan of the instrument. Yet another issue is the temperature gradient across the sample that is associated with most of the "mini furnace" setups, which require special detectors and stages for observation.

1. Protochips

Recently, a company called Protochips, Inc. (Raleigh, NC) has delivered a product that alleviates many of these problems in HTSEM. Their line of products for *in-situ* testing has revolutionized the field, specifically in the degassing, thermal electron rejection by the detector, and temperature gradient areas during observation. Their products allow *in-situ* observations to be recorded while providing the sample with heat, electrical, pressure, electrochemical, atmospheric, and liquid stimuli.[67, 68]

II. EXPERIMENTAL PROCEDURE

A. Spinel Synthesis and Reduction

Samples were prepared as described in previous works.[10–12] In brief, $NiAl_2O_4$ with 2.5 wt. % ZrO_2 was calcinated at 1500°C from appropriate mixtures of NiO (97%, Arcos Organics), α-Al_2O_3 (99%, Fisher Scientific), and $ZrO(NO_3)_2 \cdot 6H_2O$ (99%, Aldrich Chemistry) by a wet impregnation method. Loss on ignition was previously calculated and accounted for by thermogravimetric analysis. Samples were milled with Al_2O_3 media in deionized water for 30 minutes, and subsequently dried overnight. Calcination of the spinel was performed at 1500°C for 8 hours, with a furnace heating rate of 5 K/min in air. Cooling of the furnace to room temperature occurred at the same rate. Grinding of the synthesized spinel was done in an alumina mortar and pestle until being able to pass through a 297μm sieve, U.S. number 50. X-ray diffraction was tasked with ensuring the correct phases of spinel and ZrO_2 were present for the $NiAl_2O_4$ + 2.5 wt. % ZrO_2 composition. Small amounts of residual NiO were present, approximately 0.5 wt. % determined by XRD.[10]

Spinel reduction was performed in a previous work.[10, 28] A charge of 3.30 ± 0.001g of calcinated spinel was placed in high alumina crucibles (CoorsTek, Golden, CO) and positioned in a furnace below an S-type thermocouple for temperature measurement. After evacuation to a pressure of 0.1 Torr, a heating rate of 3 K/min was applied until the specified reduction temperature was achieved. Once the target temperature was achieved, the furnace was backfilled with 40 ± 0.4 kPa of ultra-pure H_2, measured by a capacitance manometer. Reduction for 29 and 12 hours were performed at temperatures of 750 and 900°C respectively. Times were determined in a previous study,[10] using high temperature X-ray diffraction in a N_2 + 4% H_2 reducing atmosphere until the Ni reflections ceased increasing. Upon cooling at a rate of 3 K/min, the furnace atmosphere was maintained until room temperature was achieved.

B. *In-situ* High Temperature X-ray Diffraction

In-situ high temperature X-ray diffraction (HTXRD) was done in a custom Bruker D8 Advance equipped with an Anton Paar HTK 1200 XRD furnace using Cu Kα radiation on the 900°C reduced sample. Two experiments were conducted in air and N_2 atmospheres to assess the effects of oxygen on regeneration and stability. Air was introduced at a flow rate of 150 ml/min to provide an oxidizing atmosphere. Industrial grade N_2 (5-20 ppm pO_2, 1 atm reference) was used to investigate a low pO_2 atmosphere. Pattern collection parameters and heating profiles for these two experiments were identical. Patterns were collected over an angular range of 12.5° 2θ using a Vantec linear position-sensitive detector, allowing rapid *in-situ* measurements to be made. Scans from 25-105° 2θ were performed at a scan rate of 0.5° 2θ/s, step size of 0.025° 2θ, and a count time of 0.05 sec/step resulting in a collection time of 160 seconds per pattern. Figure 2 shows the temperature profile for HTXRD experiments. Patterns were collected at room temperature (RT), then from 400-1100°C in 100°C increments, and finally again at RT after cooling at 0.5 K/s. A heating rate of 0.5K/s was used throughout the analysis, with 1 hour dwell times before each pattern was collected to equilibrate the system. Analysis of the X-ray patterns was performed using the Bruker-AXS EVA and Topas software.

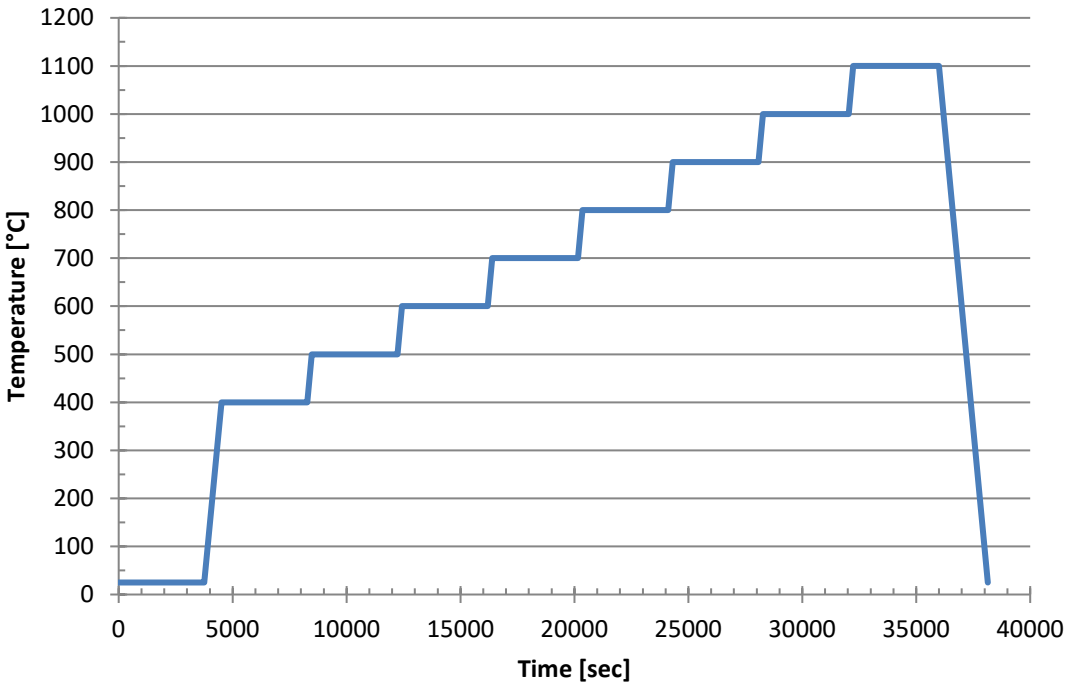

Figure 2: Temperature profile for air and N_2 HTXRD experiments.

C. Scanning Electron Microscopy

1. Alfred University

All standard scanning electron microscopy (SEM) performed at Alfred University was conducted in a JEOL JSM 7800-F (JEOL, Tokyo, Japan) field emission electron microscope. Accelerating voltages between 2.00 and 15.0 keV were used to obtain the electron micrographs, depending on application. Samples were imaged on a carbon planchet which was loaded by depositing a suspension of powder and ethanol and subsequently drying the sample. A coating of Au-Pd was necessary for accelerating voltages above 6.00 keV.

2. Offsite SEM

SEM was also conducted using a Hitachi S-3400 variable pressure SEM located at Oak Ridge National Laboratory (see Acknowledgements), using low accelerating potentials ranging from 0.20 to 6.00 keV. No conductive coating was necessary due to the low accelerating voltages.

3. Powder Cross Sections

Powder particle cross sections of the 900°C reduced and re-oxidized spinel were prepared by suspending the spinel in epoxy, approximately 5 vol. %. The suspension, as well as extra epoxy, was then placed in a Buehler Cast n' Vac 1000 system to minimize bubble evolution during the pouring process. Sample mounts were ground using SiC paper, starting at 300 grit and using progressively smaller grit sizes. The final stage used a 1 μm polycrystalline diamond polishing finish. Epoxy mounts were then cleaned with acetone and ultrasonicated in ethanol for 20 minutes to remove residual polishing media from the surface. Conductive coatings of sputtered Au-Pd were applied to mitigate charging artifacts during imaging. Imaging of the cross sections was performed in the JEOL JSM 7800-F with conditions discussed earlier in the section.

D. *In-situ* Low Voltage High Temperature Scanning Electron Microscopy

In-situ low voltage high temperature scanning electron microscopy (HTSEM) was performed in a JEOL JSM 7800-F equipped with an Aduro hot stage system (Protochips, Raleigh, NC). The Protochips stage, controlled by Aduro 200 V2.2.4 software, was connected to a Keithley Model 2611B power supply (Tektronix, Beaverton, OR) via a pass-through port on the SEM chamber door. Heat is delivered to the sample by means of a semiconductor device (E-chip) which has a carbon film that dually acts as both heating element and support. The active area upon the chip consists of a 7x7 grid of 5.5 μm holes spaced such that they cover an area 100x100 μm in size. To obtain accurate temperatures (within ±10°C), only the center 3x3 grid of holes is used. The small heating element enables manufacturer quoted heating rates of up to 1000 K/ms to a maximum temperature of 1200°C within this central area of approximately 40x40 μm. Providing heat over the small element makes it possible to image the sample *in-situ* at elevated temperatures without specialized detectors; thus, standard high sensitivity detectors may be used during high temperature imaging with minimal risk of damage to the electronics. Furthermore, the E-chip offers good thermal stability and manageable beam drift during imaging.[67–69]

Figure 3 shows the heating grid of the E-chip with the reduced spinel particles dispersed on the surface. Similar particle dispersion was implemented for each HTSEM experiment. The inner square represents the region where particles were analyzed while the outer square shows the whole area heated by the e-chip.

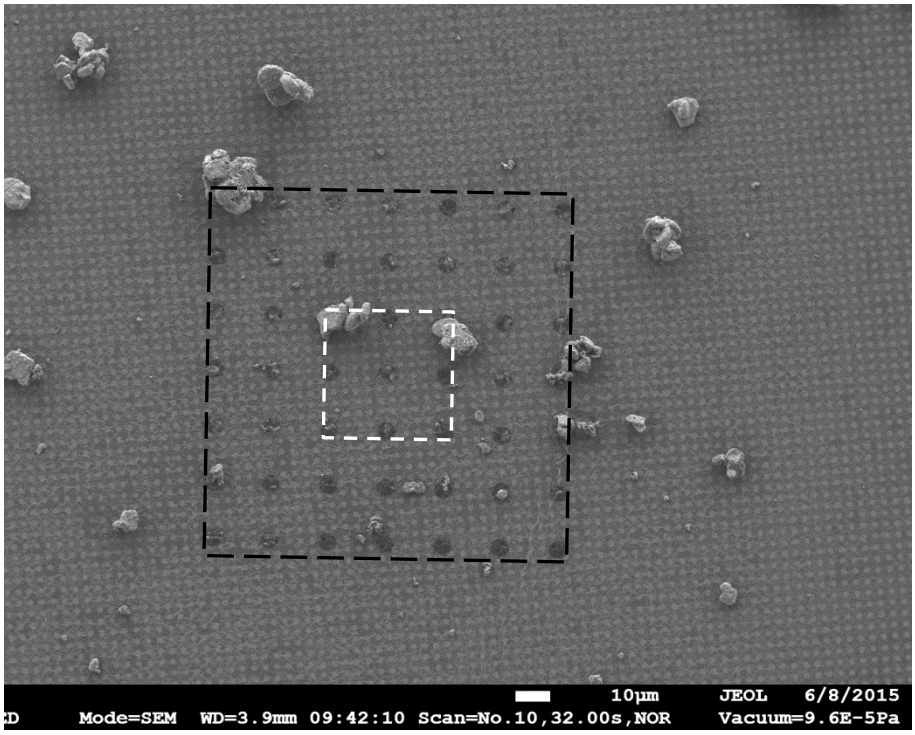

Figure 3: Heating grid for the Protochips E-chip with reduced $NiAl_2O_4$ dispersed over the grid. The center grid (inner square) and the outer grid (outer square) are marked.

Sample loading of the E-chip consisted of creating a suspension of the spinel powder in ethanol. The suspension was then deposited upon the chip by transferring a drop on the tip of a set of precision tweezers (of the kind commonly used in TEM) and subsequently drying the specimen. Optical microscopy was used to ensure powder was deposited upon the heating grid before loading the sample into the SEM. After the sample was loaded, external testing of the electrical connections between the chip and the sample holder were performed using a testing apparatus provided by Protochips. Failure of the connections test elicited repositioning of the chip on the sample holder. Upon passing, the holder was placed in the SEM, evacuated, and a temperature calibration file (provided for each individual chip by Protochips) was loaded for analysis.

Screen video captures were taken for the duration of heating for all HTSEM experiments to have the option of extracting individual frames. Open source video software provided by CamStudio (V. 2.7.2) was used for recording. A Python (V 2.7.8, Anaconda Distribution V 2.3.0, Spyder 2.3.4 GUI) module, moviePy (V 0.2), was used to compile and edit the raw data into a video synchronized with the time and temperature recorded by the Protochips software. Video editing was done in such a way to compress the time scale of the video from an hour to a few minutes. Example code for video editing can be seen in Appendix 1 – Python Code.

1. High Vacuum

Conditions for the HTSEM experiments consisted of imaging with a 2.0 keV accelerating potential with a working distance of 4mm at a base pressure of $9.634 \cdot 10^{-5}$ Pa ($pO_2 \approx 2 \cdot 10^{-10}$, reference 1 atm) of air to avoid using a conductive coating that could alter the *in-situ* observations. Three recordings were collected; two with the 900°C reduced sample and another with the 750°C reduced sample. All heating rates were controlled via a computer interface using the Aduro software. The first recording of 900°C reduced sample consisted of a ramp rate of 5K /s from RT to 1100°C where a hold for just over 81 minutes was performed (Figure 4A). From 1100°C to RT, the maximum cooling rate (1000K/ms) was applied. Another investigation exposed the 900°C reduced sample to a more controlled heating rate shown in Figure 4B. This consisted of heating from RT to 200°C at the maximum rate, then to 500°C and 600°C pausing 150s, 84s and 46s respectively to adjust microscope focus, brightness and contrast. From 600 to 1000°C, a ramp rate of 5K/s was applied with a hold at 1000°C for 592s. The same heating rate of 5K/s was applied to increase the temperature from 1000 to 1100°C. 1100°C was maintained for 6780s and then the maximum rate was applied to cool to RT. The heating profile (Figure 4C) for the 750°C sample consisted of heating to 200°C, 400°C, 500°C, 550°C, 600°C, 700°C at the maximum rate, pausing to adjust focus, brightness and contrast. From 700 to 1150°C, the temperature was increased by 50°C increments and pausing to adjust, then holding at 1100°C for 720s and at 1150°C for 1920s. All experiments were performed with rapid heating to gain an understanding of the kinetics of the passivation process at 1100°C compared to HTXRD. Two experiments used a low

magnification to provide an understanding of the overall change in the number fraction of catalyst particles, the spatial variation in number fraction over the substrate surface, and morphological changes of the substrate material. The controlled heating experiment was performed at high magnification to observe the local interactions between the catalyst particles and the substrate.

2. Low Vacuum

A recording experiment in a variable air atmosphere (10-60 Pa, 20-124 ppm atm pO_2) was conducted using an accelerating potential of 6.0 keV without a conductive coating as well as a working distance of 5.3mm. The temperature profile (Figure 4D) consisted of a ramp at the 4K/s to 700°C, back to 500°C to adjust for contrast and brightness, then a computer controlled manual ramp to 845°C, where the experiment was aborted.

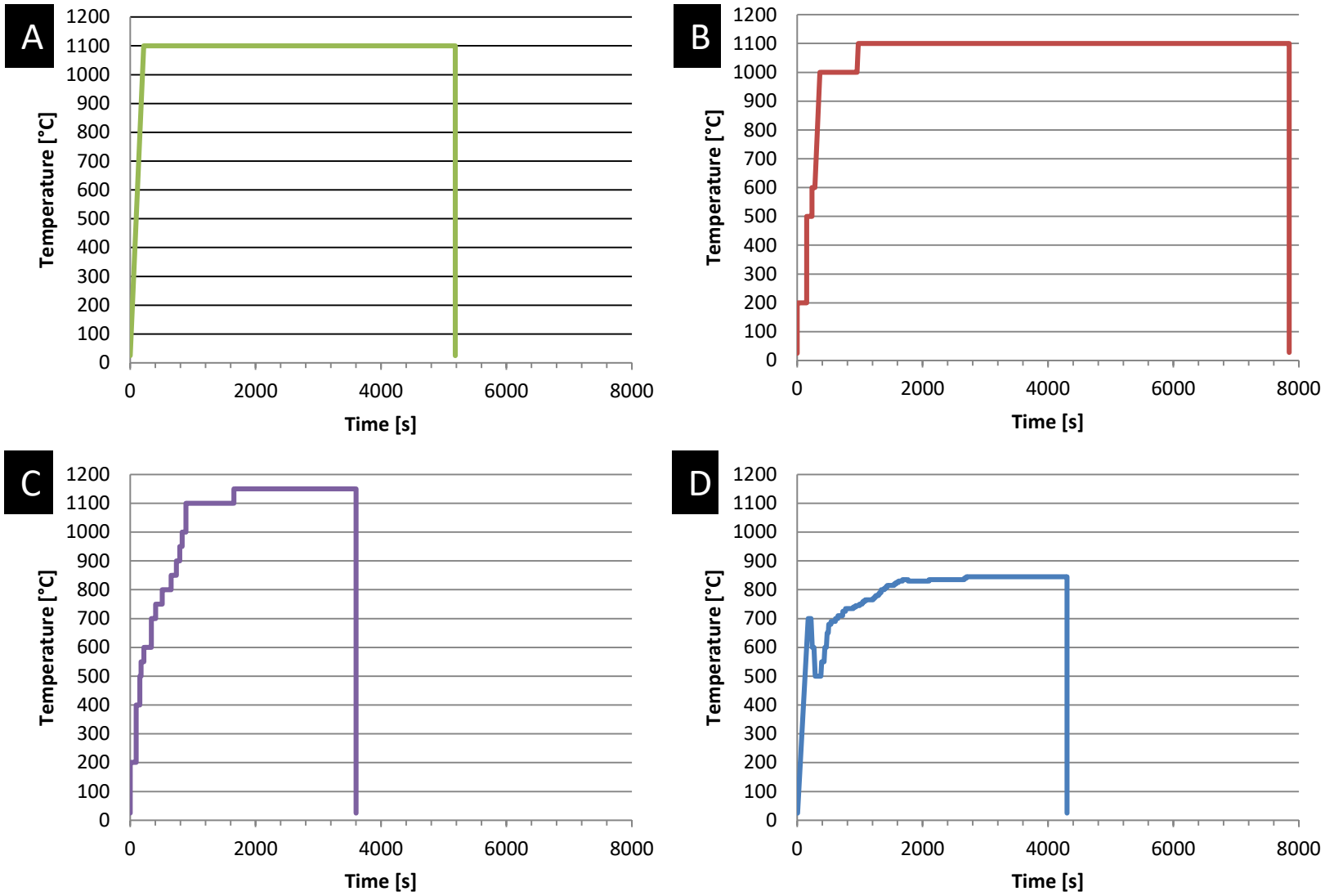

Figure 4: Temperature profiles for *in-situ* HTSEM: A. High vacuum low magnification (25kx) on 900°C reduced $NiAl_2O_4$. B. High vacuum high magnification (50kx) on 900°C reduced $NiAl_2O_4$. C. High vacuum low magnification on 750°C reduced $NiAl_2O_4$. D. Low vacuum experiment on 900°C reduced $NiAl_2O_4$.

E. *Ex-situ* High Temperature Scanning Electron Microscopy

1. Low Pressure

Ex-situ SEM was also performed on the 900°C reduced spinel before and after a heat treatment was applied on the Protochips stage. Heating was applied in a controlled air atmosphere inside the SEM chamber of 45 Pa, approximately 100 ppm atm pO_2. Images were collected before and after the heat treatment when vacuum was restored. The heating profile for this experiment can be seen in Figure 5 which consisted of using the maximum heating rate to 200°C, the a ramp of 5K/s to 1100°C. Temperature was maintained for an hour and then a ramp of 5K/s was applied to RT.

2. Ambient Pressure

In addition, the 750°C sample that was oxidized *in-situ* was studied via *ex-situ* HTSEM. Exposure to heat treatments consisted of the same heating rate as the *ex-situ* low pressure experiment holding for 1 and 4 hours (Figure 5). Cooling to RT was conducted at the same rate as heating. The long holds at temperature were performed after bringing the SEM chamber to ambient pressure and therefore ambient pO_2. Vacuum was restored for imaging after both 1 and 4 hour holds.

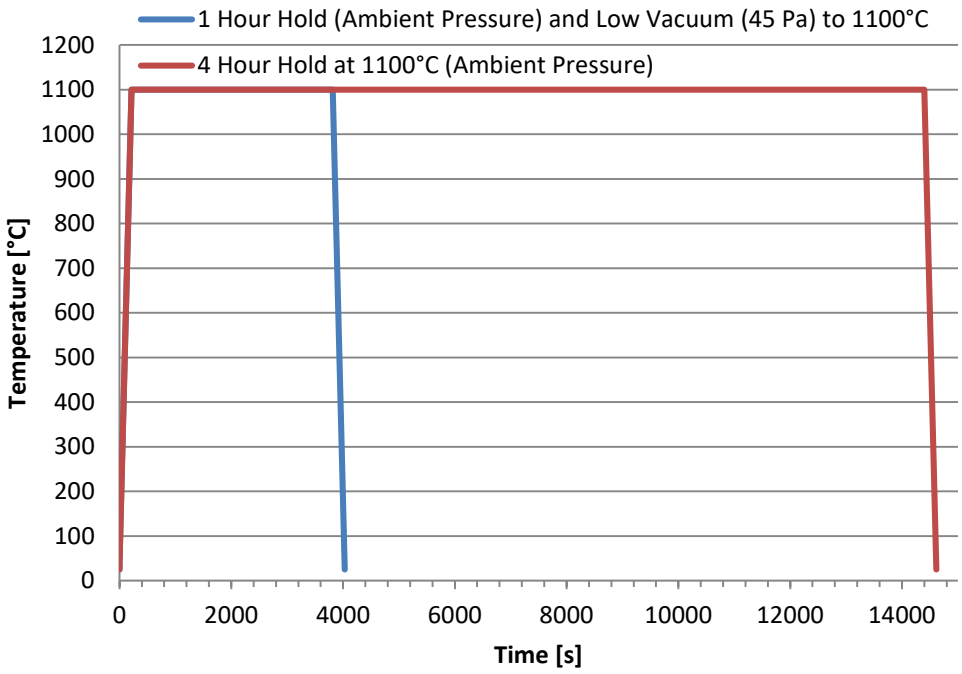

Figure 5: Temperature profiles for the ex-situ heating experiments.

F. Electron Backscatter Diffraction

Electron backscatter diffraction (EBSD) was performed on oxidized and both reduced (750 and 900°C) powder samples, as well as cross sections of the 900°C reduced sample for a total of four samples. Powder sample preparation consisted of loading a carbon planchet with the powder suspended in acetone and subsequently allowing the suspension to dry. An Au-Pd coating was applied for 30 seconds to mitigate charging effects. An accelerating potential of 15 keV, sample tilt of 70°, and a working distance of 15mm were used for pattern collection. Data collection and analysis were conducted using EDAX OIM suite, V 7.1.1 (EDAX Inc., Mahwah, NJ).

EDAX software uses the Hough transform for analysis, which can be adjusted to detect and identify bands according to the sample characteristics. Hough parameters for band detection consisted of a bin size of 120, 1° theta step, maximum peak count of 7, a minimum peak count of 3, with the Classic+ Hough parameters at high resolution. Hough peak identification parameters consisted of using a 9x9 (medium) convolution mask, a minimum peak magnitude of 7, a maximum peak magnitude of 10, peak symmetry of 0.50, and a top vertical bias of 11%. Camera settings and image processing refine the collected image of the pattern to be processed by the Hough transform, making detection and identification accurate. Camera settings consisted of 2x2 binning (resolution of 324x244), a gain of 190 dB, and exposure of 2.5 seconds with no snapshot or scan frame averaging. Image processing of the obtained pattern consisted of a 10 frame background capture, with background division, normalization of the intensity histogram, and finally a median smoothing filter which were applied in that order.

Finally, a phase was constructed due to the lack of a nickel aluminate ($NiAl_2O_4$) phase within the OIM database. Using data from previous work,[11, 70] a phase was now created to index the patterns collected. The parameters used for phase generation are shown in Table II.

Table II: 900°C Reduced $NiAl_2O_4$ Structural Parameters for EBSD Phase Construction

Symmetry	**Space Group**		**Lattice Parameter [Å]**		
cubic	$Fd\bar{3}m$, No. 227		8.048		
Occupancy			**Positions**		
Al	Ni	O	x	y	z
0.58	0.42	0.0	0.5	0.5	0.5
0.85	0.15	0.0	0.125	0.125	0.125
0.0	0.0	1	0.2251	0.2251	0.2251

III. RESULTS AND DISCUSSION

A. *In-situ* X-Ray Diffraction

1. HTXRD on $NiAl_2O_4$ + 2.5 wt. % ZrO_2: Flowing Air

900°C reduced $NiAl_2O_4$ + 2.5 wt. % ZrO_2 was examined by HTXRD during exposure to air flowed at 150 ml/min to track the phase changes the catalyst undergoes during heating. Patterns are shown in Figure 6 according to the temperature profile in Figure 2. This highlights the transition of Ni to NiO and regeneration of the parent spinel phase. The temperature profile used in this experiment mirrors the HTSEM experimental temperature profiles (Figure 4), in terms of maximum temperature in an attempt to closely correlate any temperature induced phase changes. As shown in Figure 6 $NiAl_2O_4$ spinel, Ni metal, tetragonal ZrO_2 and Baddeleyite (monoclinic ZrO_2) phases are present at room temperature of the reduced spinel. Bunsenite (NiO) peaks form in the temperature range of 400-500°C. Full oxidation of Ni to the Bunsenite phase occurs from 800-900°C. Residual amounts of the NiO peaks are still visible in the room temperature pattern after heating. The spinel peaks sharpen as the temperature increases, indicating regeneration of the phase. Baddeleyite and tetragonal ZrO_2 phases show no change in peak intensity and no secondary phases are formed which is in accordance with the available phase diagrams[71–73] (shown in Appendix 2 – Phase Diagrams). No solubility of the ZrO_2 with the spinel, Ni or NiO phases is observed with HTXRD. The final room temperature scan shows peaks of spinel, the two ZrO_2 phases, and remnant NiO that has not yet recombined to form $NiAl_2O_4$.

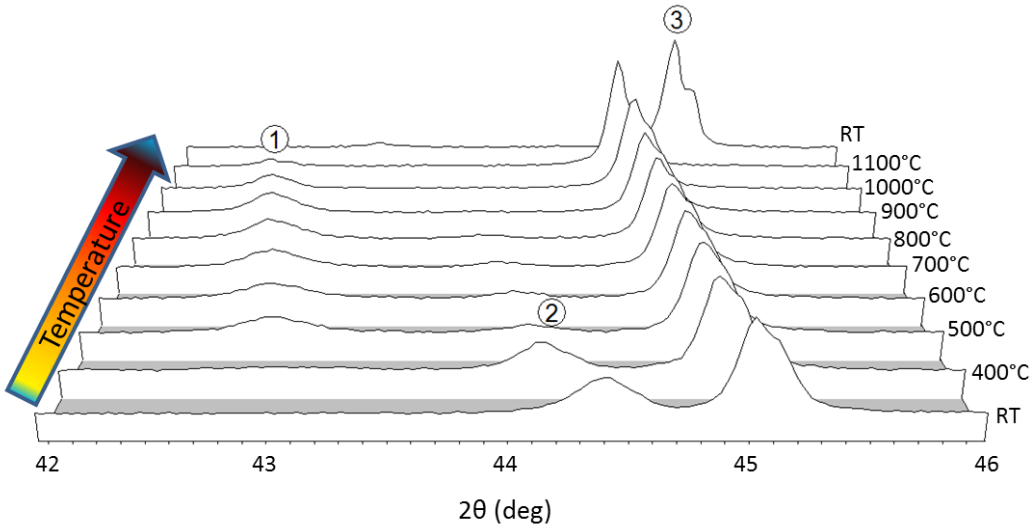

Figure 6: *In-situ* HTXRD patterns in flowing air of a previously reduced $NiAl_2O_4$ catalyst. Phases identified in the patterns are Bunsenite (after 400-500°C), Ni (until 500°C) and $NiAl_2O_4$ spinel with the corresponding principle peaks labeled as 1, 2, and 3 respectively.

2. HTXRD on $NiAl_2O_4$ + 2.5 wt. % ZrO_2: N_2 with Trace pO_2

HTXRD under a blanket gas, industrial grade N_2, was performed on previously reduced $NiAl_2O_4$ + 2.5 wt. % ZrO_2 at 900°C to evaluate stability under an atmosphere of low pO_2, approximately 5-20 ppm atm. A gas flow rate of 200 ml/min was utilized with a temperature profile mirroring the previous HTXRD experiment in flowing air (Figure 2). Patterns are shown in Figure 7. Initially, as expected, phases present were identical to the initial patterns for the oxidizing experiment, due to the same starting sample with no reflections of NiO. No θ-alumina or corundum phases were present, indicating that the spinel is stable under these conditions up to 1100°C. An increase of the spinel peak intensities also occurs upon cooling indicating the regeneration of the parent spinel phase.

Investigation of the reduction of $NiAl_2O_4$ + 2.5 wt. % ZrO_2 has been performed previously.[11] It has been shown that $Ni_XMg_{1-X}Al_2O_4$ spinel is unstable under long holds at elevated temperatures.[28] Specifically, the X = 1 composition, $NiAl_2O_4$, becomes unstable between 900°C and 950°C with the formation of metastable alumina phases such as θ-alumina. Long holds with limited pO_2 (reducing conditions) force Ni extraction from the defect spinel, and subsequently through a phase transformation to higher alumina polymorphs such as θ and α-alumina, which are detrimental for regeneration due to the lack of a close-packed oxygen sublattice. Since these previous works investigated the stability under reducing conditions, it was necessary to investigate the spinel stability under a higher pO_2.

HTXRD data under N_2 shows that with 5-20 ppm pO_2 introduced upon heating, the spinel is stable up to 1100°C. Available Ni-NiO phase equilibrium diagrams and the Ellingham Diagram[32–36] indicate that NiO formation should occur under these conditions, but was not observed in this investigation. Intensity increases observed in the spinel peaks indicate that some NiO is reincorporated into the defect spinel at high temperatures. Formation and reincorporation may occur at similar rates at lower temperatures which may explain the absence of any NiO reflections. The XRD investigation suggests that the oxidative transition occurs following the equation:

$$NiAl_2O_4 \xrightarrow{H_2+heat} Ni_{1-x}Al_2O_{4-x} + xNi + \frac{x}{2}O_2 \xrightarrow{O_2+heat} xNiO + Ni_{1-x}Al_2O_{4-x} \xrightarrow{time+heat} NiAl_2O_4. \quad (9)$$

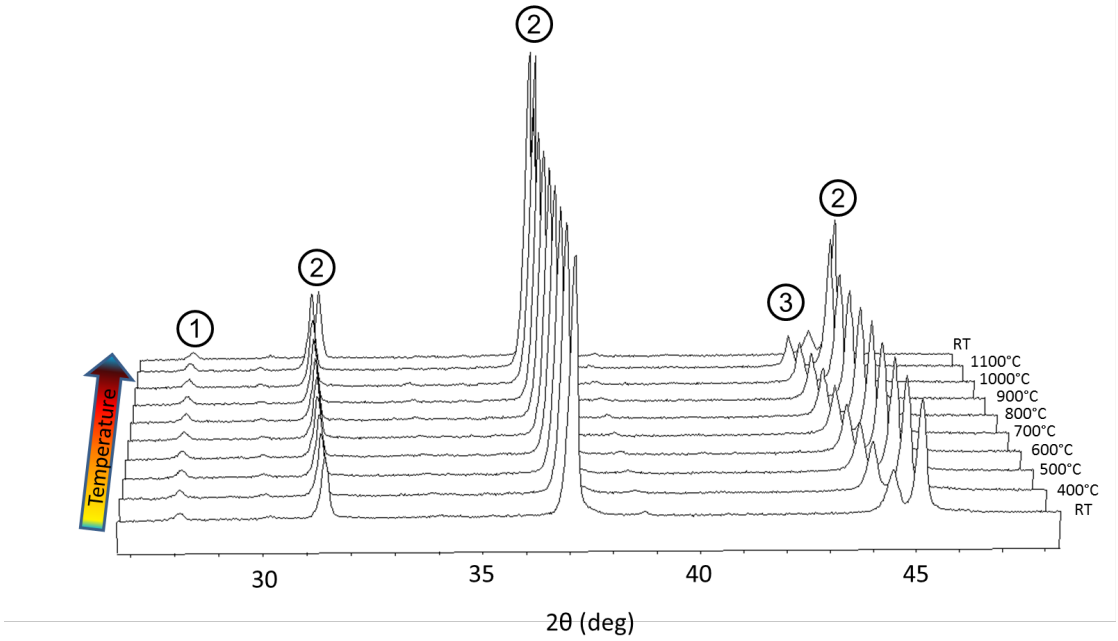

Figure 7: *In-situ* HTXRD patterns in flowing N_2 of a previously reduced $NiAl_2O_4$ catalyst. Phases identified are Baddeleyte (ZrO_2), $NiAl_2O_4$, and Ni, labeled 1, 2, and 3, respectively.

B. Microstructural Evolution of Surface and Bulk

1. Surface Evolution

Surface microstructural evolution of the reduced $NiAl_2O_4$ was evaluated with respect to temperature. Samples reduced at 700°C, 750°C, and 900°C under 40 kPa of He + 4% H_2 were investigated and characterized via SEM. Figure 8 shows the reduction temperature with the corresponding variations in surface microstructure, specifically matrix surface morphology, Ni particle size and Ni crystallite location upon the surface. Large spheroidal particles on the matrix are identified as the ZrO_2 matrix modifier, while the small particles are the Ni crystallites.

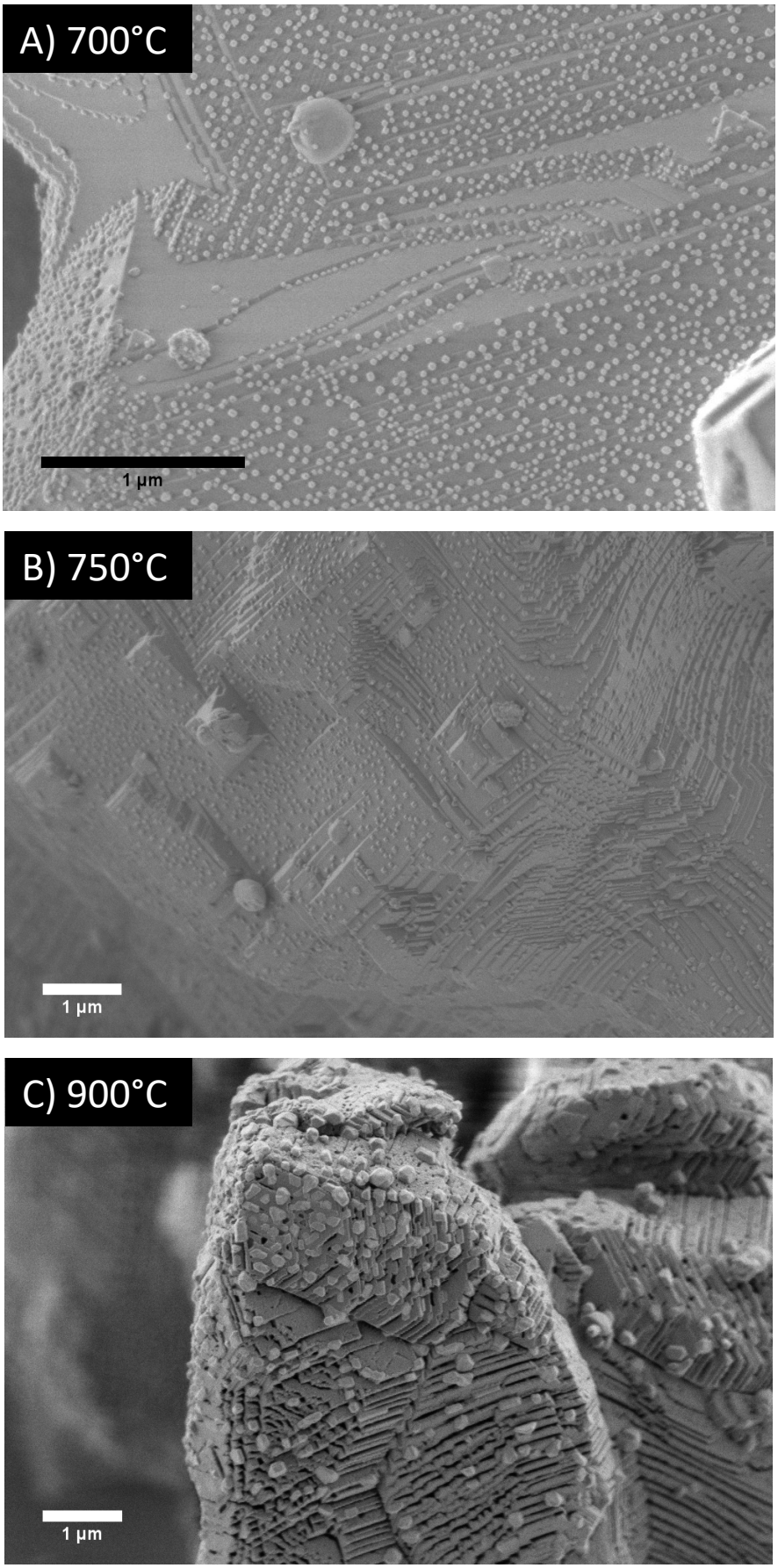

Figure 8: Micrographs of $NiAl_2O_4$ reduced at 700°C, 750°C, and 900°C, labeled A, B, and C in 40kPa He + 4% H_2 for 51, 29, and 12 hours respectively.

Before the particle shapes and sizes of the Ni crystallites can be discussed, basic understandings of the FCC type crystal shapes are in order. FCC type crystals, including Ni, NiO and the spinel phase, have well defined shapes when the system reaches equilibrium. As a general rule for FCC type crystals, $E^s_{(111)} > E^s_{(100)} > E^s_{(110)}$ for low index planes (which are typically the lowest in energy), where $E^s_{(hkl)}$ is the surface energy for the (hkl) plane, which is derived from many variations of the embedded atom model.[43–46, 48] These simulations all give different values for the surface energy of Ni, but do agree that the $E^s_{(111)}$ is the most energetically favorable of the low index planes. Ni crystallite geometries for the {111} and {100} are shown in Figure 9. The {111} plane normal orientation can be imagined as a truncated triangular shape, whereas the {100} can be visualized as a rectangular bar, or a square pyramid as the {111} planes dominate when equilibrium is approached. Crystallite faceting only occurs when sufficient temperature is reached. This temperature, called the roughening temperature (T_R) is classically around ¾ of the melting temperature. For Ni, T_R is approximately 1100°C.

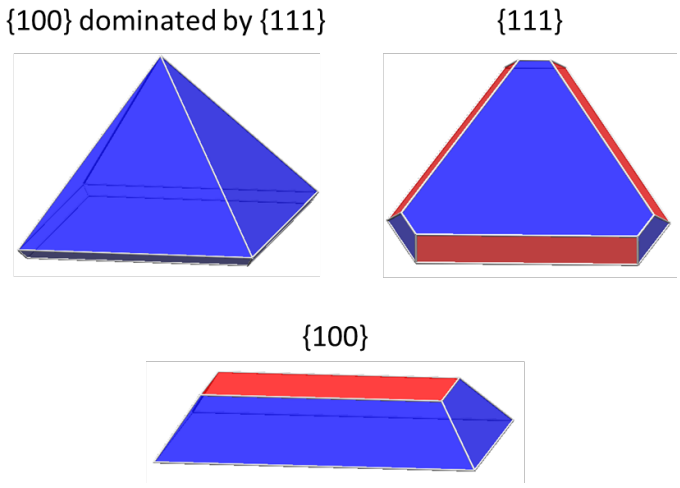

Figure 9: Equilibrium shapes of {100} (red) and {111} (blue). {100} dominated by {111} is also shown.

Figure 10 shows a SEM micrograph of extreme differences observed in Ni crystallite shape depending on surface location. Figure 11 illustrates the multiple observed shapes of the Ni particles in relation to location throughout the temperature range. Particles which reside on flat surfaces have well defined equilibrium shapes while step located particles have poorly defined morphology, resembling a spherical shape

more than a faceted crystallite. Particles located upon steps are qualitatively larger, roughly twice the size of Ni crystallites located on flat surfaces. Ni crystallites located upon ZrO_2 also have no distinct shape. Enhanced transport of the Ni particles along faceted surfaces by a surface migration and coalescence mechanism may account for the increase in crystallite size between 750 and 900°C.

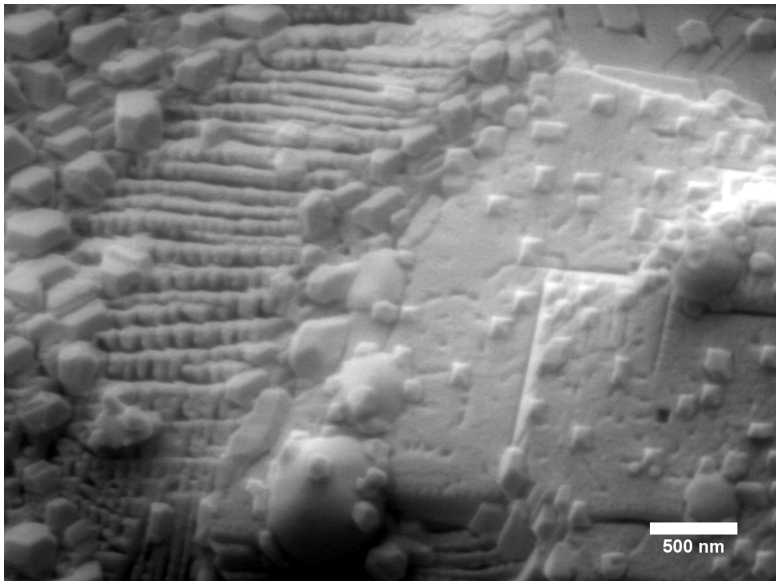

Figure 10: Micrograph demonstrating particle shape differences depending on support surface morphology.

Previous work with this series demonstrated that with increasing reduction temperature, the amount of nickel reduced from the parent spinel increases as do the crystallite sizes.[11] Changes in crystallite size with respect to reduction temperature are apparent throughout the image sequence in Figure 8. The 700°C reduced sample exhibits small (50-70 nm)[28] Ni particles dispersed throughout the structure, mostly located on surfaces that resemble steps or creases of shallow facets. An illustration is provided in Figure 11 for clarity. Very few particles are on flat surfaces, and particles do not have distinct shapes as expected since temperature of reduction for this sample is significantly less than T_R (1100°C for Ni). Reduction at 750°C yields a larger amount of Ni crystallites with sizes (45-70 nm)[28] and shapes similar to the 700°C sample, as expected in accordance with T_R. Ni particles are now located on both steps and to flat surfaces indicating that migration of the particles occurs to some degree at this temperature, and implying that particle surface transport begins to occur at 750°C. Although some

migration may occur, particles are well dispersed throughout the structure and the same size as the 700°C sample indicating that coalescence does not occur below 750°C. It is of note that at these reduction temperatures the spinel surface morphology is unchanged, with a large amount of faceting still present with no pitting or crevasses.

$NiAl_2O_4$ reduced at 900°C is drastically different from the previously discussed samples. Ni crystallite size is noticeably larger than that of 700°C and 750°C reduced samples (100-250 nm)[28] while a decrease in number density is observed. Surface diffusion and coalescence of small particles with increased temperature is the hypothesized mechanism for this observation, indicating that this process occurs between 750 and 900°C. The larger particles located on flat surfaces begin to exhibit equilibrium shapes of {111} and {100} planes as the roughening temperature of Ni is approached, while crystallites found on faceted and stepped surfaces exhibit visually unidentifiable morphologies. The support surface is also roughened by the emergence of long shallow crevasses traversing the surface, presumably due to diffusion of vacancies to the surface at temperatures above 750°C.[10, 11]

Ni particles are also located on the ZrO_2 matrix modifier, either on top of the particle or in contact with the surface of both matrix and modifier for all temperatures investigated. Crystallite sizes of the Ni particles located on ZrO_2 are consistent with those on the matrix.

In conclusion to the surface analysis, lower temperatures provide small undefined Ni crystallites on matrix faceting and ZrO_2-spinel interfaces, while higher temperatures increase the crystallite size and define shapes based upon location. This is important in regards to catalytic activity; it is known that points on a crystal are more catalytically active than facet edges and planes. More under coordinated sites is hypothesized to increase catalytic activity and TOFs.[12] Crystallite size is attributed to nickel diffusion along the surface at elevated temperatures. Equilibrium shape of the crystallites occurs when the temperature approaches T_R for flat surfaces, while particles exhibit undefined faceting when located upon stepped surfaces.

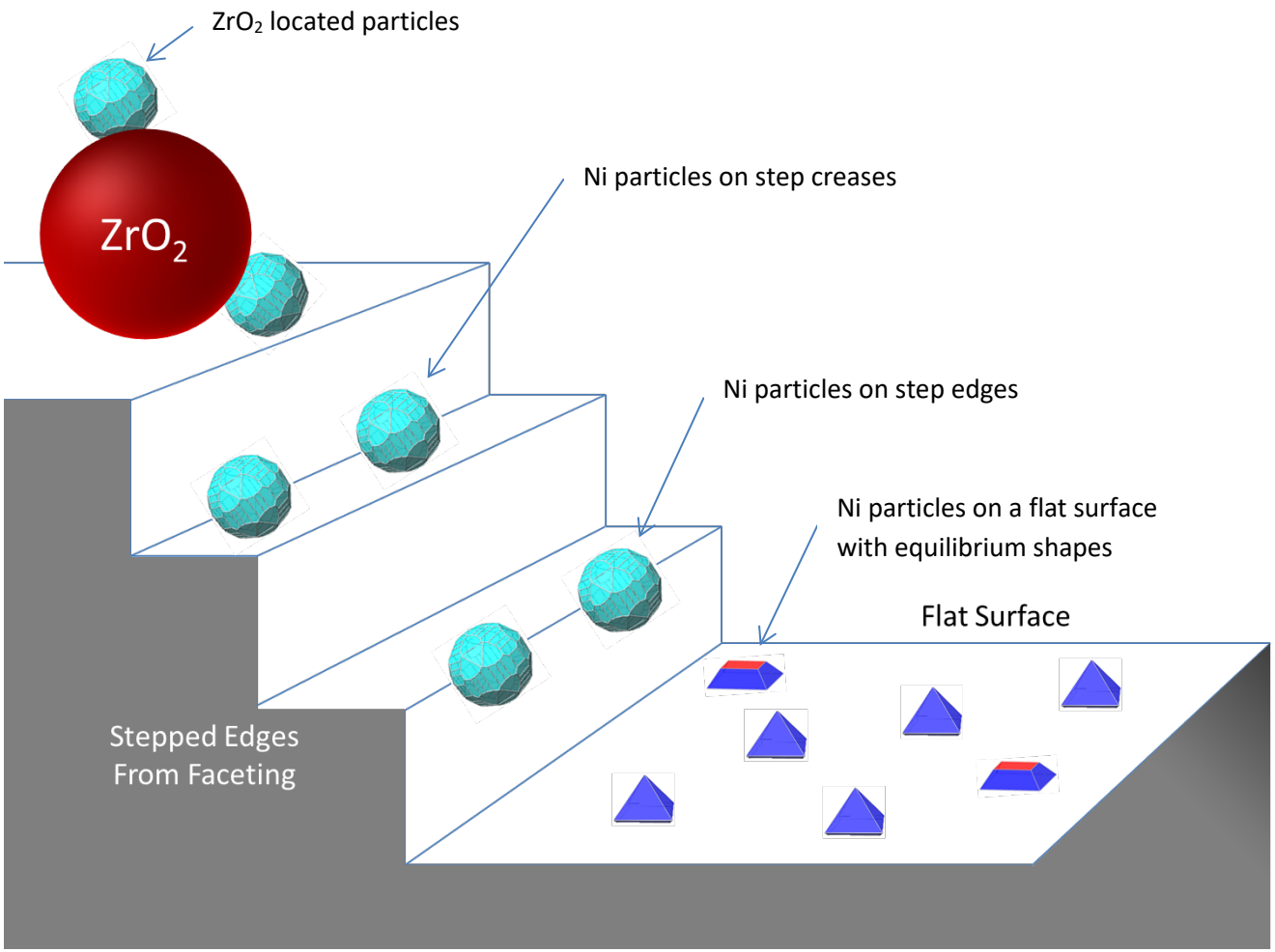

Figure 11: Illustration of Ni particle location and shape according to position upon the surface. Morphologically undefined particles are shown to be on surface facets, primarily on step edges and creases and on ZrO_2. Equilibrium shapes are shown to be smaller and on flat surfaces.

2. Bulk Characterization

To determine the internal microstructure and the nature of diffusion through the spinel bulk, cross sections of reduced (900°C) and re-oxidized $NiAl_2O_4$ + 2.5 wt. % ZrO_2 were studied.

a. Reduced Cross-Sections

The internal microstructure of the reduced sample can be seen in Figure 12. Bulk investigations reveal long needle-like features embedded within the matrix. These needle features have either parallel or regularly intersecting orientations occurring at approximately 60°. The regular intersection angles and existence of parallel features imply that these do not occur along grain boundaries, but rather intragranularly. Needle-like features of this nature have been reported elsewhere in the literature as reduced metallic Ni for this system,[28, 39] as well as reduced metals for other mixed oxides.[49] The structures are no more than a few micrometers in length and vary between 10-70 nm in width. Cracking is observed throughout the structure up to 2-3 μm deep into the particle, with the number density of the features increasing toward the surface. Crack density is the highest at the surface presumably due to the short diffusion distance of the reducing species, allowing reduction and cracking of the surface to occur before diffusion to the bulk can occur. The observed cracking is presumably due to the reduction in lattice parameter upon extraction of the Ni^{2+} and O^{2-} from the spinel upon reduction.

The needle-like features observed are most likely caused by a combination of diffusion along dislocations and crystal imperfections (short circuit mechanisms), grain boundary diffusion, and diffusion through the observed crack network. Grain boundary diffusion may play a role for larger polycrystalline particles; however, most particles are assumed to be monocrystalline due to their size. It is of note that these features are observed in 2D; therefore the needle-like features described is indicative of a plate-like morphology in 3D. This geometry is theorized, and was not confirmed. Short circuit mechanisms are a likely cause for internal reduction and the formation of the needle-like features due to faster diffusion along crystal imperfections comparted to bulk diffusion. To better characterize this microstructural phenomenon, Rodgers and Trumble have defined a homologous temperature, T_H, which is the ratio of reduction temperature and

the melting temperature of the parent oxide.[49] In their study, they show that when T_H is greater than 0.5, ordered microstructures occur, creating uniformly distributed metallic particles as in the NiO-MgO series investigated. Below this temperature, thin elongated crystallites form from diffusion along dislocations and cracks, creating a non-homogeneous microstructure. In the case of $NiAl_2O_4$, the reduction temperature of the cross sectioned particle was 900°C, while the melting temperature of the spinel is known to be 2110°C, resulting in a T_H ≈0.43. This indicates that the microstructure of the reduced spinel should be non-uniform and contain elongated metallic crystallites, which concurs with the observations presented.

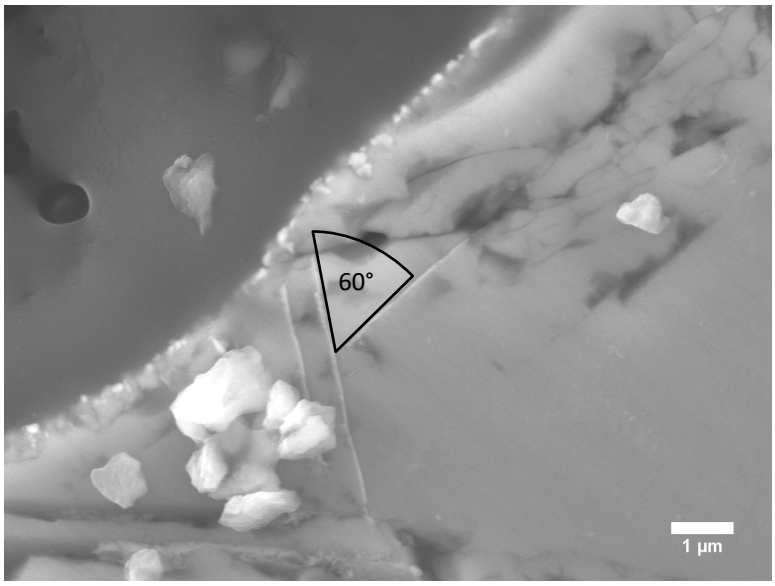

Figure 12: Image of the internal microstructure of reduced $NiAl_2O_4$. 60° intersection of the needle-like structures is shown. Large (≈1 µm) light particles are identified as residual polishing media.

Üstündag et al. observed "rod-like" Ni structures in a monolithic $NiAl_2O_4$ matrix modified with ZrO_2 reduced at 1100°C (T_H ≈ 0.52).[39] The homogeneity of the matrix is not commented on, but it is noted that the matrix can be classified as a "Ni poor" defect spinel with microcracking around the rod-like structures. Microcracks along the structures are indicative of volume reduction when Ni^{2+} and O^{2-} are extracted from the matrix, creating vacancies on both sites, resulting in a defect Al-rich spinel.

b. Re-oxidized Cross-Sections

Re-oxidized catalysts were examined to determine the changes in the bulk from reduced to oxidized states. Figure 13 shows the re-oxidized catalyst, mounted in epoxy. Residual NiO was found within some particles, consistent with the presence of remnant NiO peaks observed in the oxidizing HTXRD experiment under flowing air. Needle-like features are not present upon investigation of the matrix in any of the observed particles suggesting that the features have been reincorporated into the matrix. A significant decrease in the crack network occurs upon oxidation and is shown in Figure 13; cracking is still present, but the number density is greatly reduced near the surface, to where the larger (2-3 μm) features remain near the surface. Absence of these features is presumably due to the diffusion of oxygen and therefore Ni to the bulk through short circuit and crack network routes, essentially regenerating the bulk. Therefore, the bulk of the specimen upon oxidation does not undergo any irreversible physical changes, in terms of microstructure, composition, or phase, which are supported by the HTXRD experiments. This indicates regeneration of the catalyst bulk.

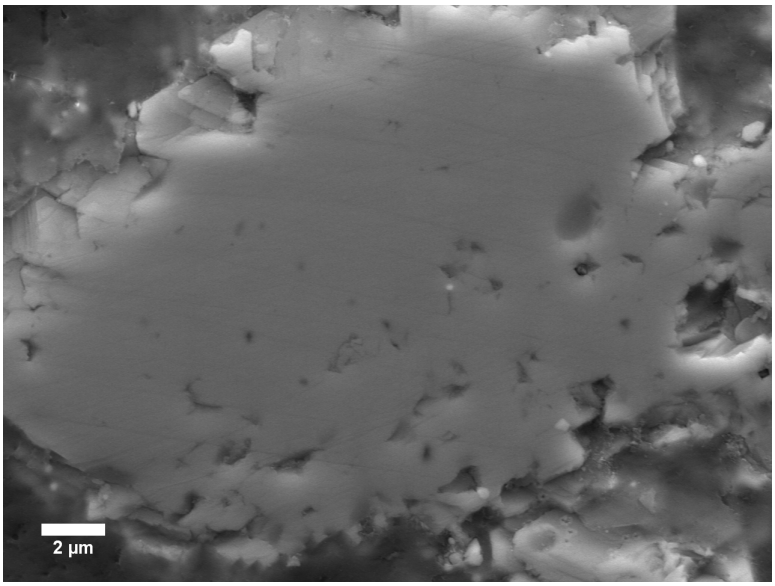

Figure 13: Cross section micrograph of oxidized $NiAl_2O_4$.

C. Low Voltage High Temperature Scanning Electron Microscopy

Several *in-situ* and *ex-situ* methods to investigate the deactivation mechanisms, specifically the interactions between the support and the Ni metal particles dispersed on the surface were performed on the catalyst. These experiments varied in SEM magnification to investigate the interactions on a micrometer (25kx) and nanometer (50kx) size scale. The effect of pO_2 within the temperature regime from RT to 1100°C was also investigated by introduction of an atmosphere while heating. It must be understood that *in-situ* observation at elevated temperatures is problematic; interactions with the atmosphere present in the chamber, thermal electron emission and deposited energy to the specimen all play an integral role during imaging. Therefore, imaging conditions are of the utmost importance in examination.

1. *In-situ* Micron Scale Observations

a. High Vacuum

The spinel was observed on a micrometer size scale to detect interactions of the reduced Ni particles with the supporting defect spinel matrix. Still images extracted from the recorded video are shown in Figure 14 with a temperature profile corresponding to Figure 4A. A reduction in the number density and an increase in mean size of the particles with time is initially observed, which is clearly seen in the first row of images. Some surface particles recombine with the spinel within a few minutes of imaging, with complete reincorporation occurring after 85 minutes of imaging, as can be seen in the last row of images. Pitting is observed in locations where particles were reincorporated into the substrate, as well as at the original locations before movement. It should be noted that no ZrO_2 matrix modifier is present on the observed particle; the modifier can be seen in the top right corner of the image sequence (Figure 14) identifiable by the spheroidal morphology.

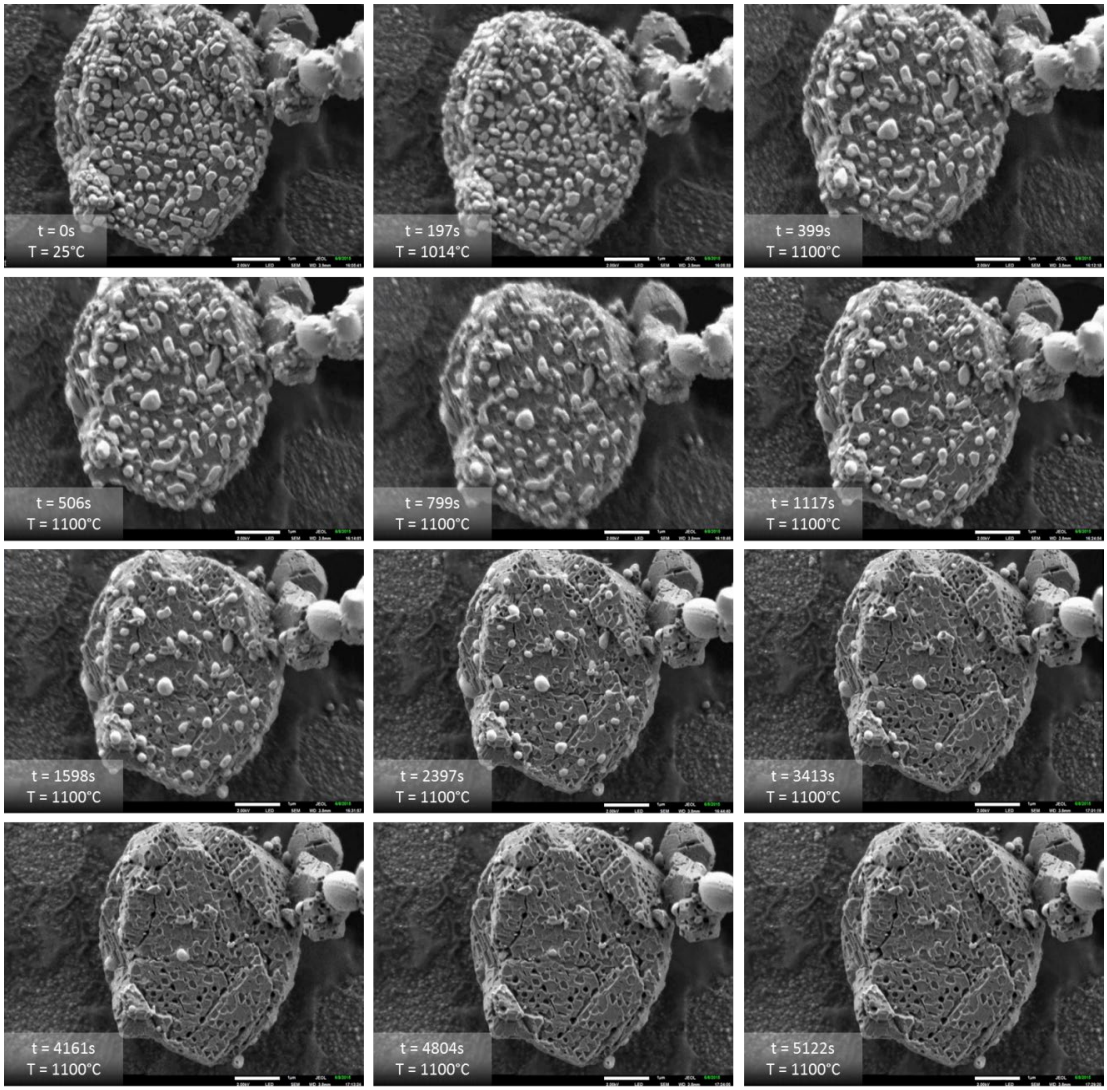

Figure 14: Shown are time lapse images from the *in-situ* high vacuum experiment on the micrometer size scale. Time and temperature are indicated in the bottom left hand corner of each individual image and go from left to right. Scale bars represent 1 µm.

The video provides direct evidence that particles migrate over the substrate surface at the base SEM pressure, $9.634 \cdot 10^{-5}$ Pa, (which corresponds to $2 \cdot 10^{-10}$ pO_2, 1 atm reference) of air at elevated temperatures. Figure 15 shows that particle migration compelled coalescence is the initial mechanism for the reduction in number density of the particles. Particles that have already migrated and coalesced appear to be randomly dispersed on the particle face, with no preferred location. Pits are observed at the previous locations of the Ni particles prior to migration as well as where the particles recombine with the matrix. Due to the rapid heating rate, the temperature at which the onset of particle movement occurs could not be determined. Since the kinetic timescale for the regeneration mechanisms is unknown, the maximum heating rate to 1100°C was used.

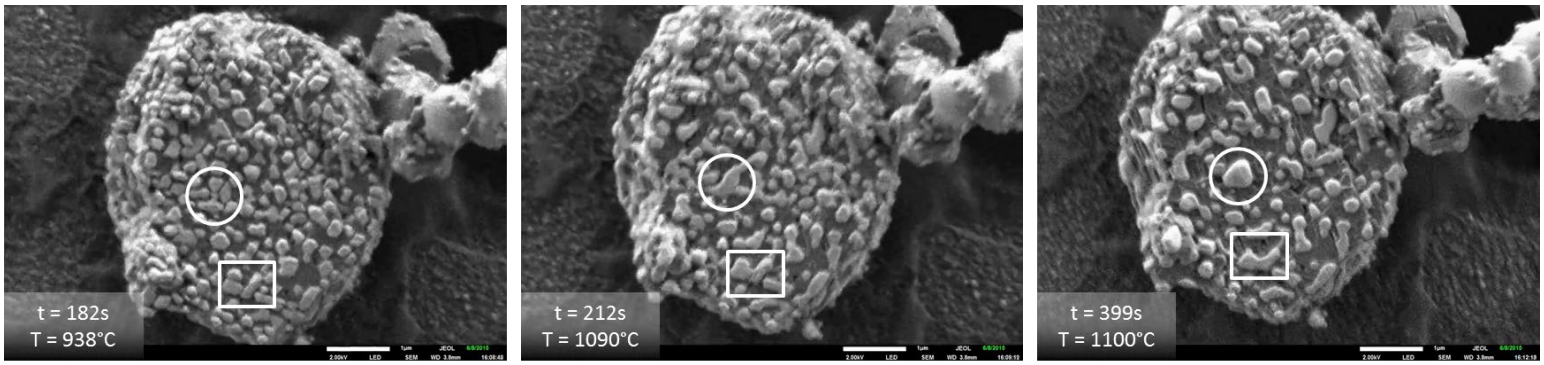

Figure 15: Time lapse image sequence from the micron scale *in-situ* experiment with the time and temperature shown in the bottom left of each image. Circles and squares highlight the coalescence of the Ni particles. Scale bars represent 1μm.

Particle migration is supported by experimental work of Hansen et al. and Sehested, who observed a migration mechanism in Pt-SiO_2 and Ni-Al_2O_3 catalysts respectively.[74, 75] Particle sizes in the aforementioned studies were relatively small (<20nm) compared to samples observed in this study (100-250 nm). Described by Wynblatt and Gjostein, particle migration can be imagined by large scale adatom diffusion along the particle surface to the edge of the particle, thus advancing the particle by one atomic layer.[76] If this process occurs frequently over a short amount of time, the particles exhibit pseudo-Brownian motion over the substrate surface with the possibility of causing collisions with other migrating particles to create large islands. It has also been shown that oxidized metals have higher surface tensions than their reduced counterparts under vacuum, indicating metals do not wet the supports like their oxide analogues.[77, 78] The particle motion over the surface is the first indication that particle composition is comprised of Ni.

The large variance (seconds compared to hours) in reincorporation rate of the coalesced Ni particles raises the question of rate dependence of particle oxidation. Larger particle sizes slow the oxidation rate by decreasing the coalesced particle surface area and by the creation of a passive oxidized shell, which is demonstrated for periods of up to 30 minutes.[79] Ni must be oxidized for assimilation into the matrix as demonstrated by HTXRD; the defect spinel must gain oxygen to accommodate incorporation of Ni^{2+} ions. Oxidation rates are also dependent on the host plane, specifically for FCC metals {111}<{110}<{100}.[47, 79–82] No determination of the faceting of the particles was possible during this experiment, nor could the phase of the coalesced surface particles be identified due to limited resolution. Therefore, a higher magnification is needed to probe nano scale features to observe particle sizes and faceting under a more controlled temperature profile.

b. Low Vacuum

An experiment was attempted using the variable pressure system of the SEM to introduce 8-10 Pa of air (pO_2 ≈20 ppm, 1 atm reference) into the chamber. Experimental design was intended to evaluate the effects of pO_2 *in-situ*, matching the HTXRD under N_2. A “white out” effect was observed the when the sample was heated to 700°C due to

thermal electron production. The hypothesized mechanism for this phenomenon is interaction of the electron beam with heated air, ionizing the molecules present, giving off electrons which flood the detector then making imaging impossible. Under normal imaging conditions at room temperature, introduction of small amounts of air into the chamber mitigate charging effects. However, at elevated temperatures, electron emission from the beam-atmosphere interaction floods the detector. This was confirmed by increasing the variable pressure to 60 Pa, which made the phenomenon more pronounced. The maximum achievable temperature for the imaging conditions was 845°C. No particle movement or coalescence was observed, presumably due to pO_2 and temperature effects.

2. *In-situ* Nano Scale Observations

To detect local interactions between the existing Ni particles, defect spinel, and the ZrO_2 matrix modifier, observation on a submicrometer size scale was used compared to the micrometer size scale of the previous HTSEM experiments. Time lapse images from the recorded video are shown in Figure 16 that correspond to the temperature profile shown in Figure 4B. Particle migration was observed over the temperature range of 900-1000°C, but not to the degree of the previous high vacuum experiment, despite being the same sample. This may be due to the faceting upon the surface providing a longer distance for the particles to migrate. Also, ZrO_2 is present, which has been found to hasten the oxidation of Ni to NiO,[83] making the reduction in surface area by migration and coalescence unnecessary for oxidation. Particles begin to reincorporate once migration and coalescence has occured above 850°C. Nanoparticles are extracted from the matrix leaving nano sized pitting between 900-1000°C after 350s of imaging. Both pit and nanoparticle features appear stable at 1000°C. This is consistent with the previous observations of pitting revealed by particle migration as well as pitting after particle reincorporation. Faceting is also visible on the receding particles, specifically at t = 855s and T = 1000°C which is approaching T_R of 1100°C for Ni, but facets cannot be identified by visual means. The dotted circle in Figure 16 shows nanoparticle emergence out of the matrix as the temperature is increased. Nanoparticle formation in surface pores is highlighted by the dotted rectangle shown in Figure 16. As the temperature is increased to 1100°C, the nanoparticles are reincorporated and matrix breakdown begins to occur.

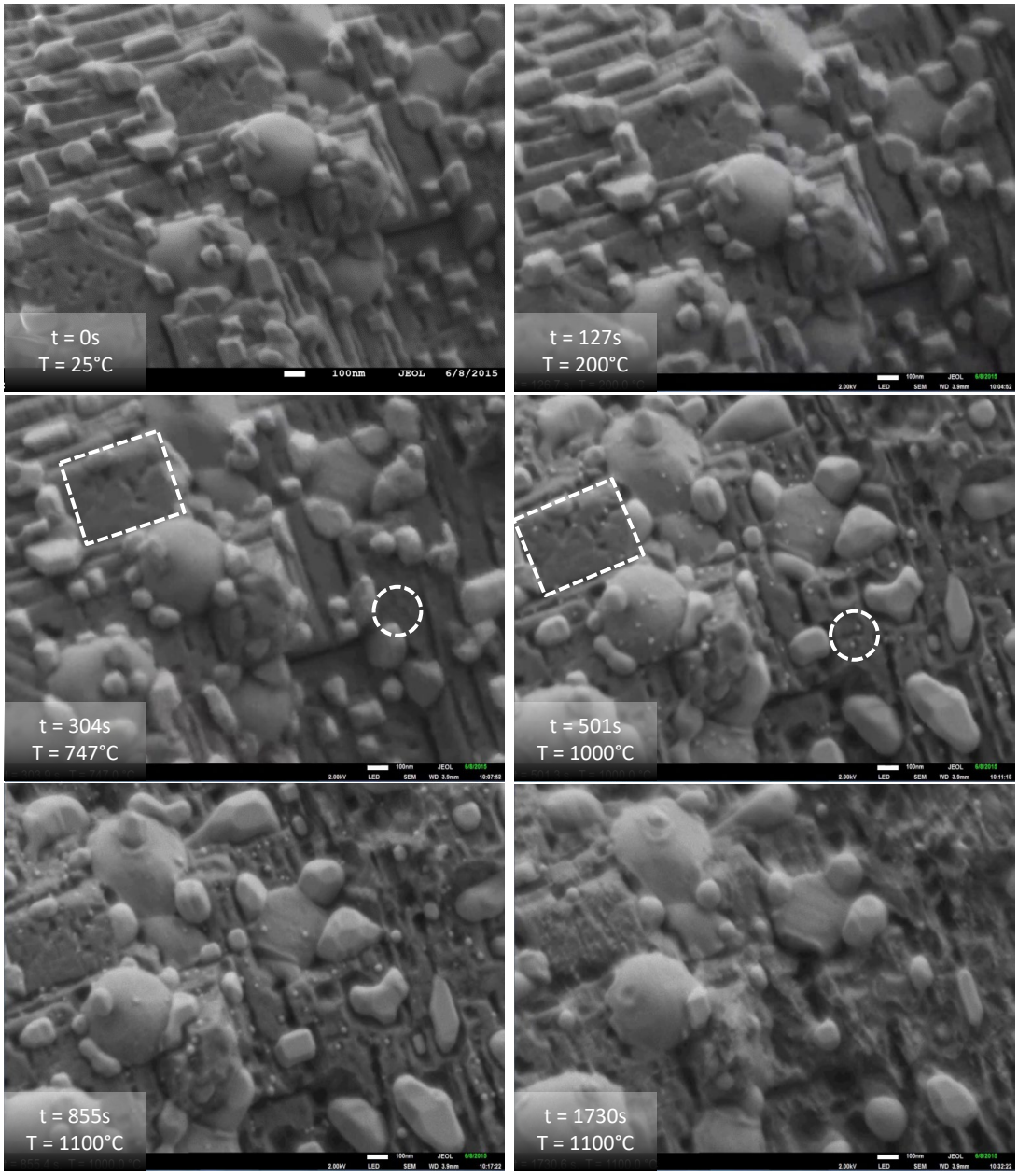

Figure 16: Image sequence extracted from the *in-situ* high vacuum experiment with corresponding time and temperatures shown in the bottom left of each image. Nanoparticle evolution can be seen at 1000°C and is highlighted by a dotted circle and rectangle. Matrix degradation is observed in the last image of the sequence.

Nano scale *in-situ* HTSEM observations on the 900°C sample reduced under ultra-pure H_2 show that surface particle movement and coalescence occurs in the temperature range of 900-1000°C at a pO_2 of $\approx 2 \cdot 10^{-10}$ atm, which is the same order of magnitude as the expected service pressure, $\approx 1 \cdot 10^{-10}$ atm. The temperature range agrees well with the Ni particle size comparison of the surface evolution with respect to reduction temperature. No migration or coalescence was observed during the low vacuum experiment described earlier, despite reaching the temperature range identified for this mechanism. This suggests that the mechanism is governed by pO_2 within the chamber. Gravity apparently has negligible effects on the particle movement; the video shows particles traversing the surface in opposite directions one would expect under gravitational influence. At the testing conditions in HTSEM under high vacuum, Ni and NiO are still solids and not liquids according to the binary phase diagram.[71] Surface tensions of Ni and NiO indicate that if a surface diffusion mechanism is responsible, migrating particles are not oxidized.[77, 78] Calculated phase equilibrium diagrams in the literature[32, 34–36] confirm that below 1000°C at a pO_2 of $\approx 2 \cdot 10^{-10}$ atm, NiO is thermodynamically favored over the reduced metal, indicating oxidation. HTXRD oxidation experiments in air clearly show that from 900-1000°C no Ni peak is present, suggesting that the surface nanoparticles which are observed to migrate and coalesce in the HTSEM experiments are NiO in the solid state. However, at lower pO_2 (from the HTXRD experiment in N_2), very small amounts of NiO are formed when 1100°C is reached, while none is formed between 900 and 1000°C. Due to the low pO_2 in the HTXRD experiment under N_2, NiO formation may be kinetically limited or the reflections may be below the signal to noise ratio of the experiment. Another hypothesis is that the NiO formation and reincorporation have similar rates; therefore the NiO is consumed to regenerate the spinel phase. However, enough NiO is formed after cooling from 1100°C to have a detected reflection, due to recombination rates decreasing with temperature. This suggests that the composition of the migrating and coalescing particles at sufficiently low pO_2 is Ni or a NiO coated Ni particle, presumably minimizing surface area for oxidation.

From 1000-1100°C, all of the available phase equilibrium diagrams indicate that Ni and NiO coexist at equilibrium, but differ in exact temperature at which this is

achieved at a pO_2 of $\approx 2 \cdot 10^{-10}$ atm. The Ellingham diagram indicates that equilibrium is reached at a temperature of 1044°C for these conditions, while Taylor and Dinsdale indicate this occurs at 1055°C.[33, 34] HTXRD and HTSEM vary in pO_2 which is crucial to determining the particle composition in this temperature range. HTXRD under oxidizing and blanket gas conditions has a pO_2 which falls within the NiO region of the phase equilibrium diagram for the extent of the experiment indicating that oxidation of the Ni is occurring. HTSEM is much more complex due to the low pO_2 and traversing the phase equilibrium line. At this low pO_2, oxidation and reduction occur at the same rate when at a temperature between 1000 and 1100°C. When the temperature approaches 1100°C, Ni should, in theory, start to reduce. This subtle change was not observed in the experiment. However, nanoparticle evolution may provide a few insights.

Due to the decreased oxygen available in the SEM chamber, the residual oxidized surface particles may go through some reduction when 1100°C is reached, but this cannot be confirmed by the present HTXRD nor HTSEM results. Current conditions of the HTXRD could not achieve the pO_2 of the HTSEM experiments. The nanoparticles can be explained as either an artifact of imaging conditions of the HTSEM experiments as Ni is formed by further matrix reduction, or the redistribution of NiO prior to reduction. These two theories are supported by data gathered in HTXRD. Ni reflections do not change when heated under the N_2 atmosphere in 5-20 ppm pO_2, even when some NiO is formed. No Ni is present under flowing air conditions at 1000°C or 1100°C. This data suggests that the observed phenomenon is not temperature induced at pO_2 greater than 20 ppm. It is important to note that it has been determined previously that the samples used in this study are not fully reduced, determined by the weight percent of Ni present after reduction compared to the theoretical weight percent available for reduction.[11] This suggests that more Ni can be extracted under sufficiently low pO_2 and high temperatures as a consequence of the phase transformation. The argument for the imaging conditions artifact theory can be bolstered by the observation that nano-scale features form in the matrix where the nanoparticles originate, leaving residual nano-pitting. Similar pitting was observed in the larger particle analog after migration, demonstrating that particle and pit formation are related. It is known that Ni can be reduced directly from the spinel phase.[10, 11] The above information indicates that the nanoparticles observed are most

likely Ni particles reducing from the matrix. Once the temperature is increased above 1000°C, the nanoparticles disappear, indicating regeneration and that the spinel is stable at 1100°C and a pO_2 of $2 \cdot 10^{-10}$ atm. It has been shown that excessive reduction of the Ni from spinel can induce a phase change from a defect γ-alumina spinel structure to metastable θ-alumina and eventually to corundum for closed system reductions at 950, 1000, and 1100°C for $NiAl_2O_4$ + 2.5wt. % ZrO_2.[10, 28] However, this work demonstrates that in HTXRD studies under N_2 (5-20 ppm pO_2), this catalyst is stable up to 1100°C.

One consequence of imaging at high magnification at elevated temperatures is the breakdown of the matrix with extended exposure to the beam, even at the 2.00 keV accelerating potential which can be seen in the final (lower right) image in Figure 16. Matrix breakdown in the *in-situ* experiment at the nm scale, shown by Figure 17, was observed as the original surface Ni particles receded into the matrix. As the surface was removed during imaging for extended periods at high temperature, nano sized particles emerged from the matrix and subsequently disappear. Most of the nanoparticles observed range between 10 and 60nm. ZrO_2 particles are not affected by the beam during this experiment, but the position of the particle is observed to sink into the matrix. When the beam is focused on the modifier, the rate at which the ZrO_2 sinks is increased which was observed *in-situ* on a 750°C sample exposed to a heat treatment profile (Figure 4C shows heating profile). Beam damage was confirmed by imaging the matrix at a "fresh location" at a higher magnification to expedite the process. This in turn degraded the matrix, confirming that the beam was the culprit for the damage. Figure 17 demonstrates the breakdown of the matrix with beam exposure with the reference image extracted at t=6474s and T=1100°C, with pit dilatation occurring ≈ 300s and nanoparticle emergence at ≈ 350s after this time.

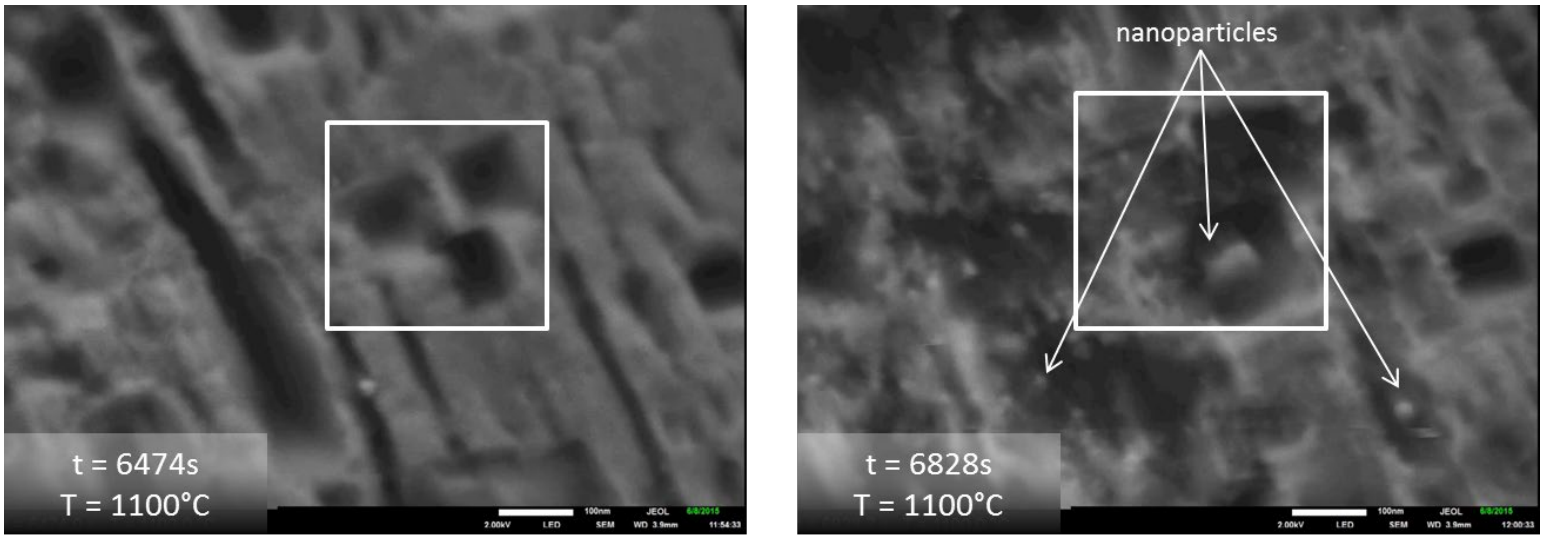

Figure 17: Beam damage of the matrix after recombination of the Ni particles is apparent. Left image is shown as the reference. The square areas represent the same location on the surface, while the nanoparticles are denoted with arrows. Scale bars represent 100 nm.

When the maximum temperature is reached for the experiment, all Ni particles recede into the matrix as time progresses, even with matrix degradation. Metal particles on the ZrO_2 modifier also disappear with increasing time. The final image in Figure 16 shows indentations on the ZrO_2 are present, and have a rounded crater-like shape dissimilar to the pitting observed on the spinel matrix. As the spinel degrades with beam interaction, the ZrO_2 morphology remains unchanged.

At the end of the heat treatment in the nano-scale observations, the matrix began to degrade with short term imaging at 1100°C. HTXRD in this study confirms that the degradation is not a phase change under oxidizing or neutral conditions. Energy input from the beam is not dismissible during the experiment and may build up enough energy to encourage a phase change, which is known to be different than heat induced phase changes[84] in high accelerating potential applications such as TEM for thin samples. No data is present on phase changes at low accelerating potentials. However, it is easy to envision that an insulating sample could create a buildup of electrons resulting in elevated energy at the surface creating a localized area where the temperature is increased. As a reference, a calculation of the maximum change in temperature at the center of the irradiated area for a stationary beam can be calculated using a modified version of Castaing's formula accounting for backscattered electron production.[85, 86] For spinel, this was roughly estimated to be 0.01°C, which is negligible for a single point. However, if this is summed over the entire scanned area, the rise in temperature may not be so small. Summation calculations of this nature are intricate and must account for multiple variables which are problematic to measure such as thermal diffusivity away from the irradiated area as well as overlap of the interaction volumes per scan point. To reinforce this theory, Joy and Joy performed a calculation showing low accelerating potentials deposit more energy per unit volume than high accelerating potentials essentially destroying the sample surface.[87] Li and Egerton estimate that a stationary probe at accelerating potentials $\leq$ 2.00 keV can result in temperature increased on the order of hundreds of degrees for polymeric materials.[88, 89] With the knowledge that metastable aluminas form when the temperature is increased above 950°C, under reducing conditions, and that reducing conditions are not met until ≈1050°C is reached, a

beam induced phase change is the most likely source of the observed surface damage but cannot be confirmed in this study.

An electrostatic buildup of negative charge may cause Coulombic interaction upon the surface, causing the jumping or hopping motion of the surface which can be observed in the recorded video. This in turn may loosen the top surface, ejecting material from the irradiated surface and depositing them elsewhere on the chip. Figure 18 supports this by showing an EDS analysis of the SiO_2 backed C support film, revealing a detectable amount of Ni and Al on the chip.

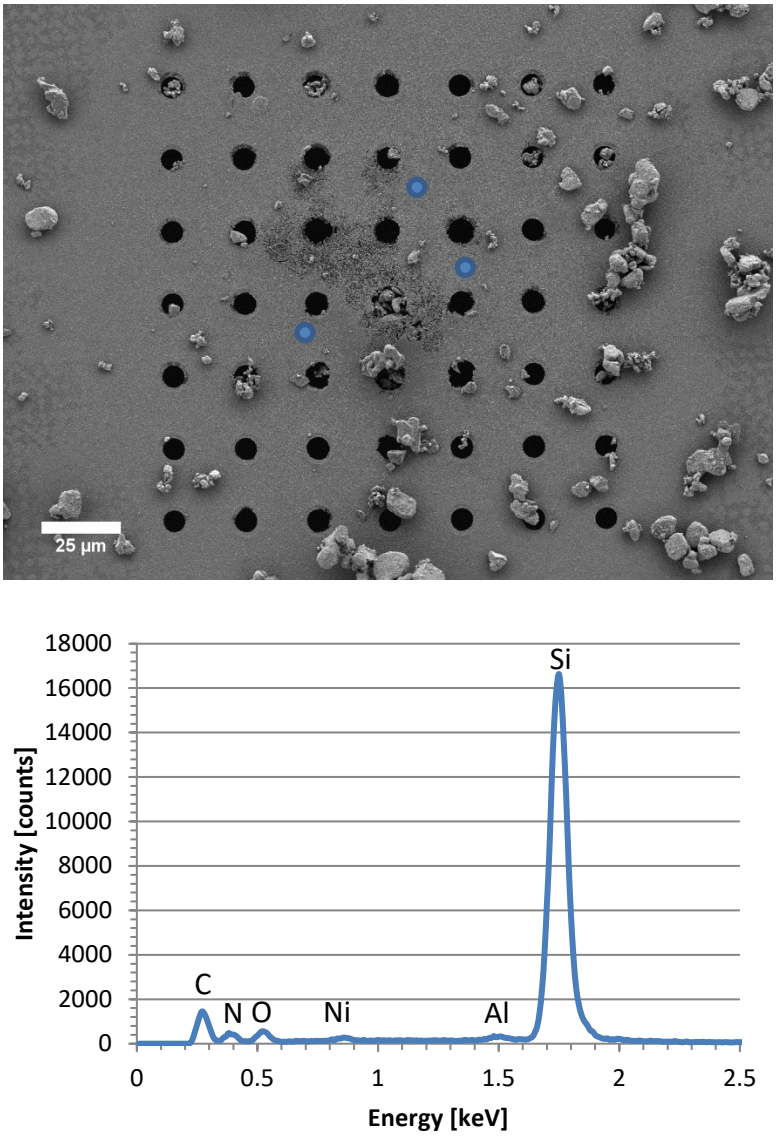

Figure 18: SEM image of Protochips heating grid with corresponding EDS spectra demonstrating Ni and Al are present on the chip in 3 locations examined by point analysis.

Another theory to the beam damage can be conceived by irradiation observation of an analog spinel, $MgAl_2O_4$, since radiation damage of $NiAl_2O_4$ is not within the literature. It was reported via EELS that atomic movement during the onset of electron irradiation show migration of the Mg^{2+} and Al^{3+} cations to preferentially occupy the octahedral sites.[90] Extending this observation to $NiAl_2O_4$, which is highly inverse compared to the normal $MgAl_2O_4$ spinel, approximately half of the Al^{3+} atoms occupy the tetrahedral site and are able to relocate to the octahedral site upon irradiation creating a deficiency of sites for migration. This shortage of sites upon irradiation may lead to subsequent breakdown of the matrix resulting in beam damage and the ejection of Ni from the matrix, in the form of nanoparticles which were observed while matrix degradation occurred, again supporting the SEM instrument artifact argument. It is of note that Al will not reduce at any conditions experienced in this study; therefore the composition cannot be Al. No conclusive evidence can be drawn from the beam damage of the specimen.

In-situ observations in the HTSEM and the HTXRD experiments presented here are forthcoming with a vast amount of detail about surface and bulk changes the catalyst undergoes during heating. Unfortunately, these techniques do not parallel each other in terms of heating rates and oxygen concentration. Due to time constraints during data acquisition, heating rates for HTSEM experiments were much higher than the heating rates for HTXRD, essentially flash heating compared to a rate of 0.5K/sec in HTXRD, with no equilibration holds in HTSEM. HTSEM requires user adjustments throughout data collection whereas HTXRD can be programmed to execute a profile and collect data with no user corrections after the initial input.

3. *Ex-situ* Heating Experiments

The previous *in-situ* HTSEM experiments were conducted in high vacuum with little oxygen present ($< 2 \cdot 10^{-10}$ atm) under testing conditions, with the exception of the low vacuum attempt. To observe the effects of an atmosphere on the oxidation and regeneration processes for the 900°C reduced sample, the partial pressure of oxygen in the SEM was increased by utilizing the low vacuum mode during heating. A controlled atmosphere of 45 Pa of air (9.5 Pa O_2, ≈100 ppm pO_2, 1 atm reference) was introduced

into the chamber while the heat treatment was performed. *In-situ* observation was not possible in low vacuum mode above 845°C due to beam-specimen and beam-atmosphere interactions; therefore an *ex-situ* method was employed to observe the surface of reduced and re-oxidized samples before and after thermal exposure.

Ex-situ observations with an air atmosphere of 45 Pa (pO_2 of ≈100 ppm) exposed for the duration of the heat treatment (Figure 5) exhibited differing behavior from the experiments performed in high vacuum for 900°C reduced samples. An oxidized sample was included with the reduced sample to investigate the effect of oxygen on the surface morphology after deactivation and re-oxidation with longer temperature exposure times. Reduced particles, upon oxidation, exhibited residual holes from the recession of the Ni surface particles similar to the vacuum *in-situ* observations, but have a larger number density with presence of a more oxidizing atmosphere. The increase in the number density of pits may be related to the oxidation of the primary surface particles, not requiring migration and coalescence for oxidation. Holes on the now oxidized spinel have shapes similar those seen in *in-situ* measurements, with geometries such as truncated squares and triangles with rounded edges. Not all Ni was oxidized and recombined with the spinel, as some NiO is observed on the surface of the support. This agrees well with the residual NiO peaks observed in the HTXRD experiment under oxidizing conditions, as well as the particle cross sections.

Figure 19 shows surface pitting of the oxidized spinel (originally reduced at 900°C), in accordance with the *in-situ* micron and submicron size scale investigations. Solid rectangles in Figure 19 highlight the sharpening of holes upon heating in an environment more conducive to oxidation. These holes tend to sharpen which results in distinctly defined geometrical forms with pointed corners and edges rather than poorly defined truncated shapes. Dotted rectangles in Figure 19 denote the disappearance of shallow faceting observed on the surface before heat treatment shown in Figure 5. These features disappear, and give way to crevasses, creating narrow elongated structures on the surface which were not observed *in-situ*. Dotted ovals highlight pitting (10s of nm) on the surface (from the exodus of the nanoparticles) which is observed to disappear after the heat treatment. A change in the location of the ZrO_2 is observed, sinking into the spinel matrix, which is denoted with a hexagon. A smoothing of the circular ZrO_2 particle is also

present, removing the crater like indentations from the surface. Ambient heating experiments on re-oxidized 750°C sample did not yield healing of the residual features on the spinel support during holds of 1 and 4 hours at 1100°C. ZrO_2 was not observed during these ambient pressure holds.

During the heat treatments, samples observed *in-situ* and *ex-situ* exhibit ZrO_2 particles receding into the matrix, which has not been previously observed or reported. Remnant craters (from Ni located upon ZrO_2) left on the modifier particles also disappear with time at high temperatures, resulting in a smooth surface. This indicates that an interaction between the matrix, ZrO_2, and atmosphere is present during the heat treatment; even when the Al_2O_3-ZrO_2 phase diagram clearly indicates that no solubility is present under these temperatures.[72] Upon further investigation, interactions with the electron beam at the elevated temperature accelerate the recession of the ZrO_2 particle into the matrix.

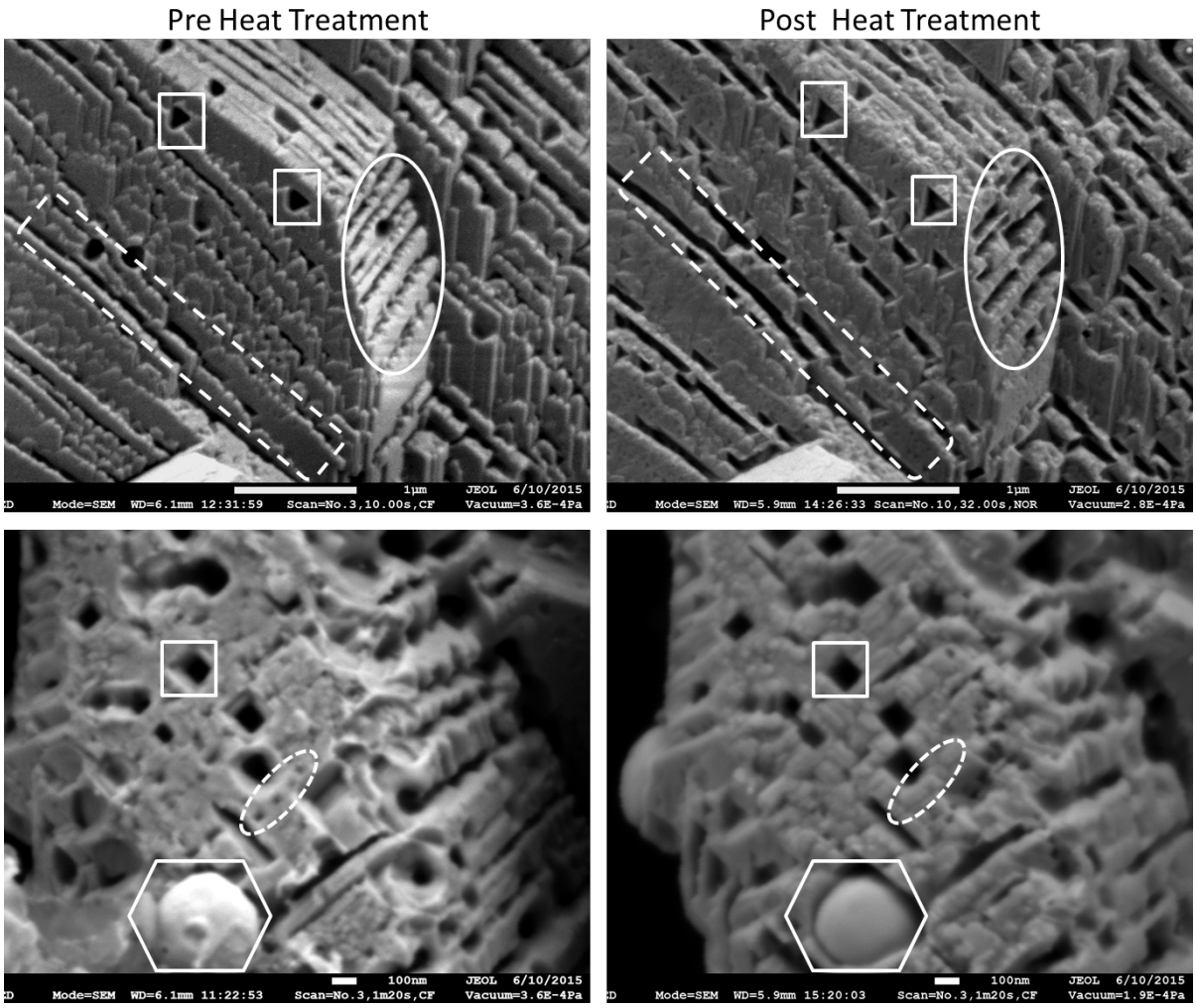

Figure 19: Shown are images from a previously oxidized sample pre and post heat treatment (left and right respectively). Marked features are discussed in the text.

Two hypotheses can provide explanations for the observed phenomenon. The decrease in lattice parameter of the spinel upon reduction may compel the round ZrO_2 particles to the surface to accommodate the physical shrinkage (up to ≈3 vol. %), and result in a crack weakened support structure below. ZrO_2 accounts for approximately 2 vol. % of the composite. Upon heating and reincorporation of Ni, the volume expansion around the ZrO_2 particle is in theory enough to allow for the observed sinking of the ZrO_2 into the surface. Electron beam interaction, specifically when the beam is focused on the ZrO_2, may increase sinking by physical and coulombic electron effects on the ZrO_2. Physical effects were found to be negligible. However, a rough calculation shows that the electronic repulsion at close distances (< 1nm) is on the same order of magnitude as the force exerted from the material, estimated through Young's modulus. The coulombic interaction between the negative surface and the negative beam creates a repulsive force that may push the ZrO_2 into the weakened support, resulting in a sinking mechanism. This theory does not account for the smoothening of the modifier in both *in-situ* and *ex-situ* experiments.

Another theory requires a vacancy approach, as ZrO_2 is a fast ion conductor via oxygen vacancy diffusion depending on crystal symmetry.[91, 92] HTXRD shows that throughout the temperature range for the experiments, tetragonal and monoclinic ZrO_2 are the phases present and do not alter with heat treatment or pO_2. Busch et al. has investigated the effect of a nanocrystalline ZrO_2 film having both tetragonal and monoclinic phases present on SiO_2[93] resulting in enhanced oxygen diffusion through the ZrO_2 layer. Enhanced oxygen diffusion to the particle interior could be explained by a dual mechanism: surface diffusion and bulk diffusion through the monoclinic and tetragonal phases, respectively. This can be applied so that at high temperatures in oxidizing conditions, the exposed surface is increased in area and the exchange of $V_O^{\cdot\cdot}$ (and therefore monatomic oxygen) among the atmosphere, support surface and the modifier occurs. This allows enhanced diffusion of oxygen to the defect spinel and Ni surface particles from the ZrO_2, regenerating the spinel phase and increasing the volume of the spinel back to the original value. As the pO_2 is fairly low ($2 \cdot 10^{-10}$ atm) in the SEM chamber, recombination of vacancies and oxygen on the ZrO_2 surface may not occur as rapidly as the diffusion of vacancies to the defect spinel-ZrO_2 interface. These processes

are independent of the electron beam and occur upon heating the sample. The mismatch in rates may create pileup of $V_O^{\cdot\cdot}$, creating positively charged voids under the ZrO_2. However, interaction with the negatively charged electrons from the beam may cause interactions with the positively charged $V_O^{\cdot\cdot}$, creating a neutral structural void and thus causing the particle to sink by charge annihilation. The craters observed after Ni particle reincorporation may be $V_O^{\cdot\cdot}$, created during Ni oxidation NiO and subsequent removal to the matrix. When the NiO is presumably recombined with the matrix by adatom diffusion, the vacancies remain, creating a crater-like indentation. If this is the case, recombination of $V_O^{\cdot\cdot}$ and oxygen may require extended time under heat especially in low pO_2 conditions, which is provided by extended holds at high temperature in a more oxidizing atmosphere. This theory accounts for the entire observed phenomena.

Features that are observed after heat treatments with 100 ppm pO_2 do not shrink with extended heat and time. Small features such as nano pitting from nanoparticle evolution and shallow faceting disappear under increased temperature and oxygen content, presumably due to either the growth of larger features or by mass transport. Observations such as these are a direct indication of surface rearrangement which demonstrates that the features are related to pO_2 at temperatures up to 1100°C. Small features (≤20 nm) may be able to recover, while larger features cannot under these conditions. It is not difficult to fathom that with a surface that has been roughened with pits and crevasses, the observed surface particle migration and coalescence phenomenon in the HTSEM will be hindered due to extended diffusion distances which diminish the effective surface diffusion, particle coalescence, and reincorporation rates resulting in comparable catalytic activity to the fresh analogue. It has been found that cycled catalysts have similar if not improved initial catalytic properties,[51, 94, 95] which also has been hypothesized as microstructural maturation.[12] The work presented here supports the maturation claim in the form of surface roughening and feature sharpening, but no distinct conclusion can be drawn. Clearly, more investigations on cycled catalyst surfaces, specifically *in-situ*, are required to arrive at a definitive conclusion.

D. Electron Backscatter Diffraction: Surface and Bulk

EBSD was utilized to obtain the orientations of the surface crystals, specifically the matrix and particle orientations. The goal of this section is to provide insight to a matrix-particle registry relationship, which is theorized to be driven by crystallography. Observation of the signal, a backscatter Kikuchi pattern or an electron backscatter pattern (EBSP) is non-trivial for this sample due to the inherent topography obstructing the backscattered electrons which generate the pattern. Factors that hinder the collection of EBSPs include but are not limited to faceting, ZrO_2 modifier particles, Ni particles, and drastic irregularities in particle shape. To decrease detrimental features and demonstrate that the technique could provide useful information, an oxidized catalyst was evaluated to verify the EBSD collection method and the generated input parameters for phase identification.

Features such as subtle surface and particle faceting, require low accelerating voltages for imaging to mitigate charging and to reduce in the interaction volume. A consequence of low accelerating voltages is a relatively weak EBSP signal. This requirement results in a slow data collection speed and long dwell times for acceptable EBSP signal-to-noise ratio. The insulating nature of the sample distorts maps due to Coulombic buildup from the long dwell times resulting in beam drift, upon where the image and resulting orientation map is warped. Therefore, reliable orientation maps could not be collected. Point analysis of the surface and particles will be presented rather than EBSD mapping due to these drawbacks.

1. Oxidized Sample

EBSD of the oxidized sample showed promising results for subsequent experiments on reduced samples. Figure 20 exhibits the oxidized sample with multiple points examined using a point analysis EBSD method. Most orientations consisted of the {111} plane family, with 60° rotations of the crystal around the <110> axis. The {111} plane normal orientations are represented with 4 point stars, while slight rotations away from this direction are signified with 5 point stars. Visual inspection of the triangular shapes upon the surface agrees with the orientations observed by EBSD. Charging is apparent for the image, even at the low accelerating voltage of 5 keV.

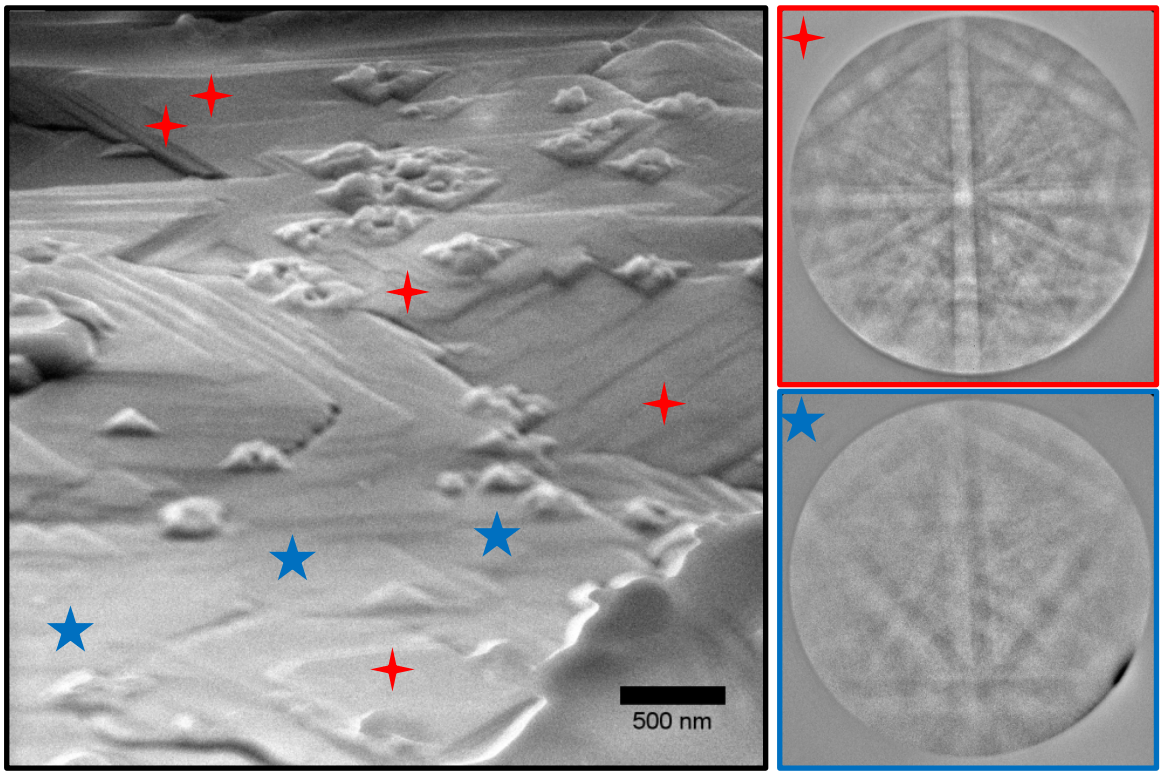

Figure 20: SEM image of EBSD point analysis with EBSP (for reference) on oxidized $NiAl_2O_4$ sample. Top EBSP pattern is {111} (denoted with 4 point stars) while bottom is slightly rotated away from this direction (represented with 5 point stars).

2. 750°C Reduced Sample

Since surface roughness is an issue, the catalyst reduced at 750°C was used for matrix-particle registry determination because of the smaller reduced Ni particle size compared to the 900°C reduced sample (45nm compared to 100nm respectively). Figure 21 shows EBSD point analysis for the 750°C reduced sample. All orientations measured for this sample consisted of {111} planes, which is in excellent agreement with visual inspection of the triangular faceting geometry as well as the embedded atom model simulations[43–46, 48] for FCC crystal low index planes. Particles are located throughout the spinel surface on facets and a few on flat surfaces, but have no specific registry to the surface {111} or {100} planes.

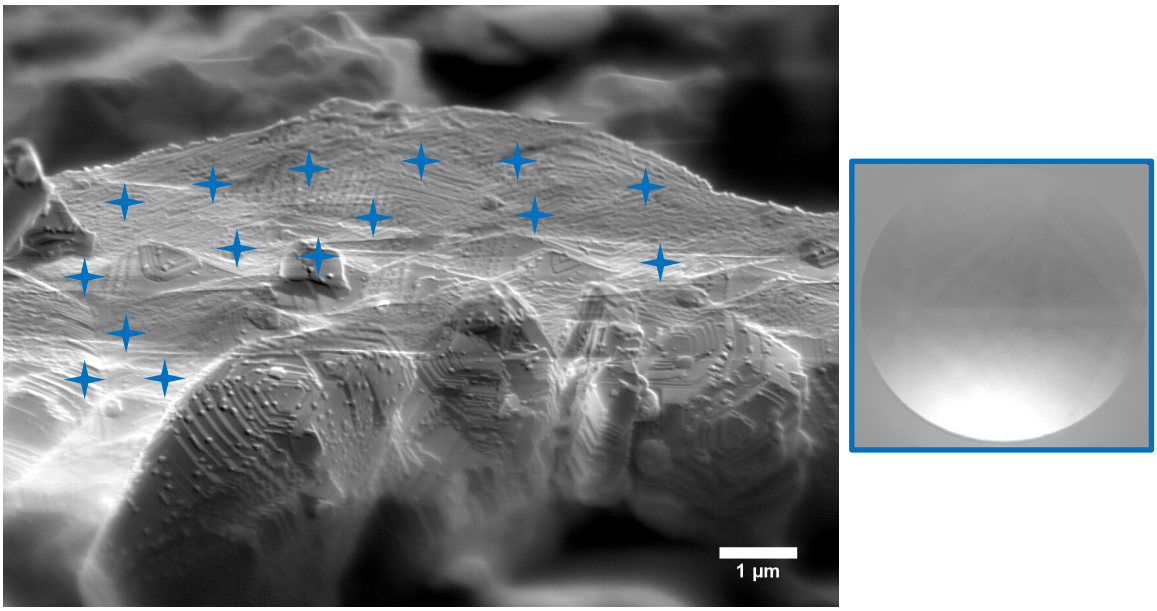

Figure 21: SEM image and EBSD point analysis for $NiAl_2O_4$ sample reduced at 750°C. Markers indicate points where orientation was measured. An example EBSP is shown for reference.

3. 900°C Reduced Sample

With successful orientations recorded from the oxidized and 750°C reduced samples, 900°C sample orientations were attempted. Fewer patterns were obtained for these experiments due to the increased surface topography resulting from the population of Ni particles which interfere with the EBSP signal. Orientations within the specimen bulk were also investigated, specifically around the needle-like features previously described.

a. Matrix and Particle Orientations

Matrix surface orientation did not vary with reduction temperature. These results are not surprising since the ceramic support was synthesized under the same conditions, but reduced at different temperatures resulting in varying Ni particle sizes. However, orientations of the 900°C matrix were recorded at multiple points on several particles, predominately consisting of {111} and {100} plane orientations, which are in good agreement with the surface faceting geometry and expected low index planes. Ni particles are approximately twice as large in comparison to the 750°C sample, 45 – 75 nm compared to 100 – 250 nm.[28]

Larger particle sizes allow for analysis to be conducted on the reduced particles on the catalyst surface by EBSD point analysis as shown in Figure 21. The particles analyzed are similar to those described earlier without equilibrium shapes due to their location upon facets. Therefore the results of the orientation of these particles cannot be confirmed by visual inspection of the faceting geometry as were the matrix surfaces. The irregular incline of the matrix faceting allowed for orientations to only be measured on three particles with EBSD. The substrate is assumed to be monocrystalline, due to the step-like faceting the particles reside on, although facets could be expected at grain boundaries. Only one pattern per particle was obtained due to this awkward geometry relative to the EBSD camera. All particles had differing orientations, indicating that the signal is in fact from the surface particles and not from the matrix, provided that the substrate is monocrystalline. Also, the surface particles have different surface normal directions indicating random orientation of the reduced surface particles on the matrix. Although orientations were collected, no distinct conclusion can be drawn with respect to

registry from these results due to the unknown sample rotation and sample surface normal with respect to the EBSD camera.

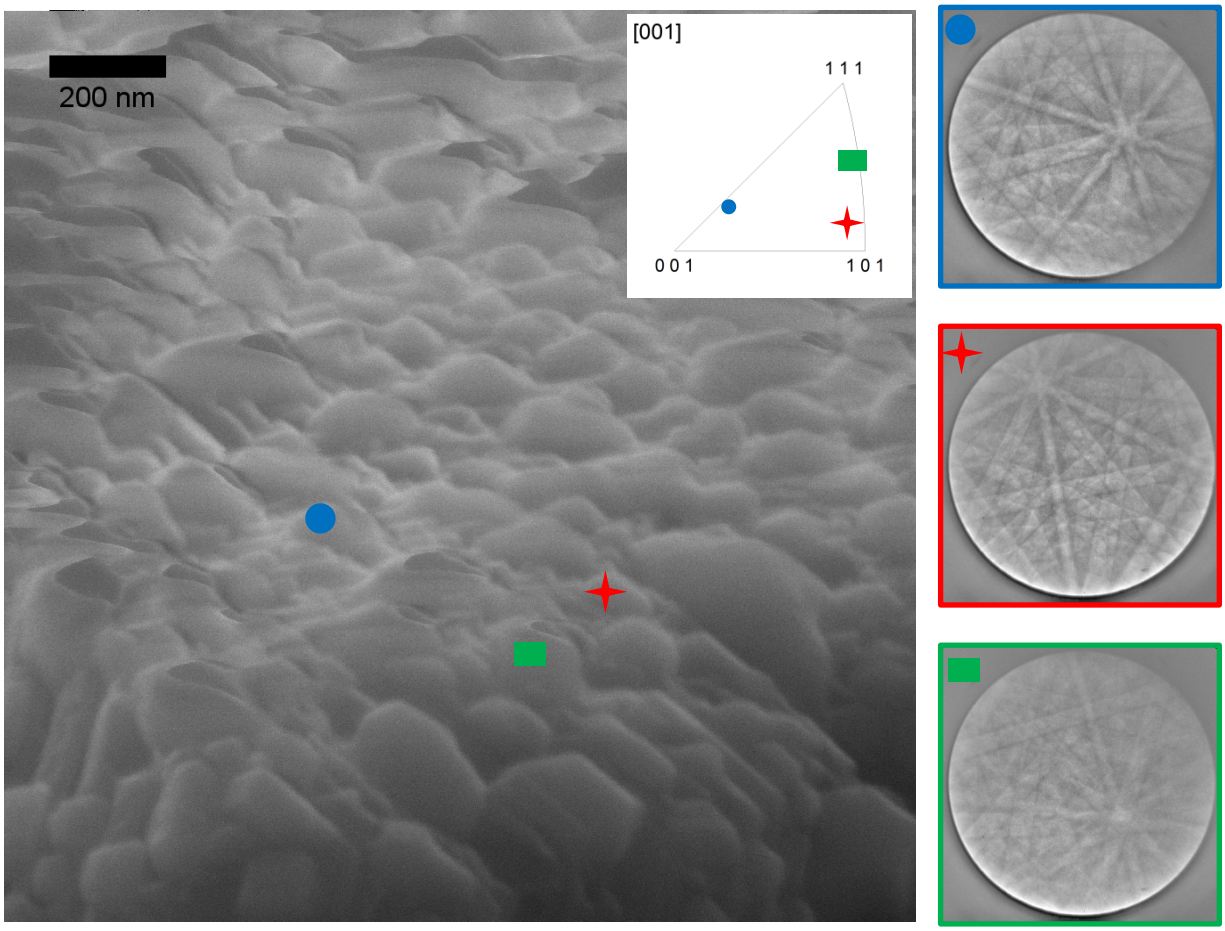

Figure 22: Micrograph of a tilted $NiAl_2O_4$ reduced at 900°C for EBSD point analysis on particles. EBSP images are shown, corresponding to the orientations measured. An inverse pole figure is provided with plotted orientations.

The results presented here are not to be taken as definitive orientations, but rather the groundwork for the technique so it can be applied to other studies if caution is taken in sample selection, synthesis, preparation, and orientation measurement. Since all particles are of irregular shape and are randomly oriented on the mount, tilt of the particle may not be exactly at 70° as by traditional EBSD software and may skew the EBSP measurement and therefore orientation. Phase identification of the surface particles based upon angles between bands was not possible because Ni and NiO share the same Bravais lattice which results in the same confidence index for both phases. Therefore, band width identification based on lattice constants is the sole way to distinguish between two similar phases.[96, 97] Both metal and metal oxide have face centered cubic structures (NiO has a rock salt structure), which are designated space group No. 225, and have similar lattice parameters of 3.524 ad 4.178 Å respectively. This results in a 15.6% increase in the lattice parameter upon oxidation. In theory, a difference greater than 10% in lattice parameters is enough to distinguish phases,[97] but pattern resolution and quality directly influence the accuracy of the phase differentiation.[96] Since the pattern quality of the EBSP is low, particle phase could not be identified by EBSD methods.

Another complication of EBSD is the information depth may include some of the matrix orientations overshadowing the surface particle patterns, creating misidentification. Classically, the information depth of EBSD is within the range of 10-50 nm.[98, 99] All three particles analyzed are larger than the 50 nm cutoff, initially indicating that the patterns are from the particles and not the matrix. However, the above statement is assuming that the particles are spherical and not irregularly shaped, as well as the interaction volume is directly under the beam. The interaction volume of EBSD is an elongated oval shape, extending “downhill” from where the beam enters the specimen. HTSEM revealed that particles migrate and coalesce, revealing pitting of the matrix from their previous locations which indicate that pitting was present pre migration, and that Ni particles resided within pits. Cross sections (Figure 12 as well as Fig. 81 in Ref. [28]) also reveal that the Ni particles are anchored into the support surface and extend deeper than the perceived surface radius of the particle resulting in oblong shapes. All of the available information suggests that the EBSP signal is in fact generated by the surface particle and

has no matrix pattern overshadowing, indicating the surface particles do not share a surface normal.

b. Matrix Orientations Around Ni Needle Features

Investigation of the needle-like features embedded within the matrix was performed via the EBSD method. The features are narrow (10-70 nm), and therefore could not be observed when tilt was applied for EBSD evaluation. An alternate approach was taken to locate the needle-like features within the matrix by a gradual tilt method, by identifying features that could be located at high tilt angles required for EBSD analysis. The sample could then be tilted incrementally and the position adjusted so that the reference points could be used to locate the approximate position of the feature within the matrix. An image taken with no tilt applied to the stage is shown in Figure 22 with arrows marking the distinct features surrounding the needle-like inclusion.

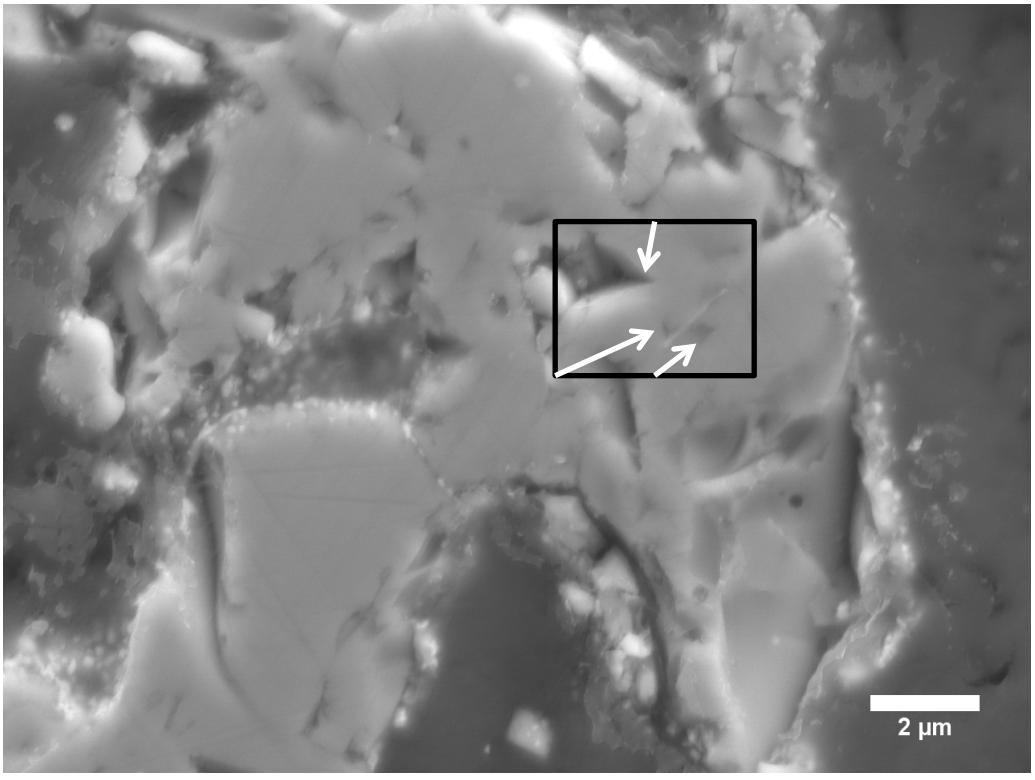

Figure 23: Micrograph of cross sectioned $NiAl_2O_4$ reduced at 900°C before tilting for EBSD point analysis, marked by the rectangle. Arrows indicate the features used to identify the location of the needle-like feature upon tilting.

Since the needle-like feature is not visible, EBSD could not be performed to determine the orientation. However, the matrix surrounding it was identified by point analysis. Figure 24 shows the cross section image at 70° tilt with points denoted where orientation measurements were taken. The location of the Ni needle by a white line, approximated from the distinct features denoted with an arrow in Figure 23. No orientation change was found across the estimated needle location. It was previously stated that the needle-like structures had regular intersection angles or were parallel features, indicating formation occurred within the grain. An absence of change in orientation across the feature supports this claim, with the needle-like features forming within the grain along crystallographic planes and not within grain boundaries.

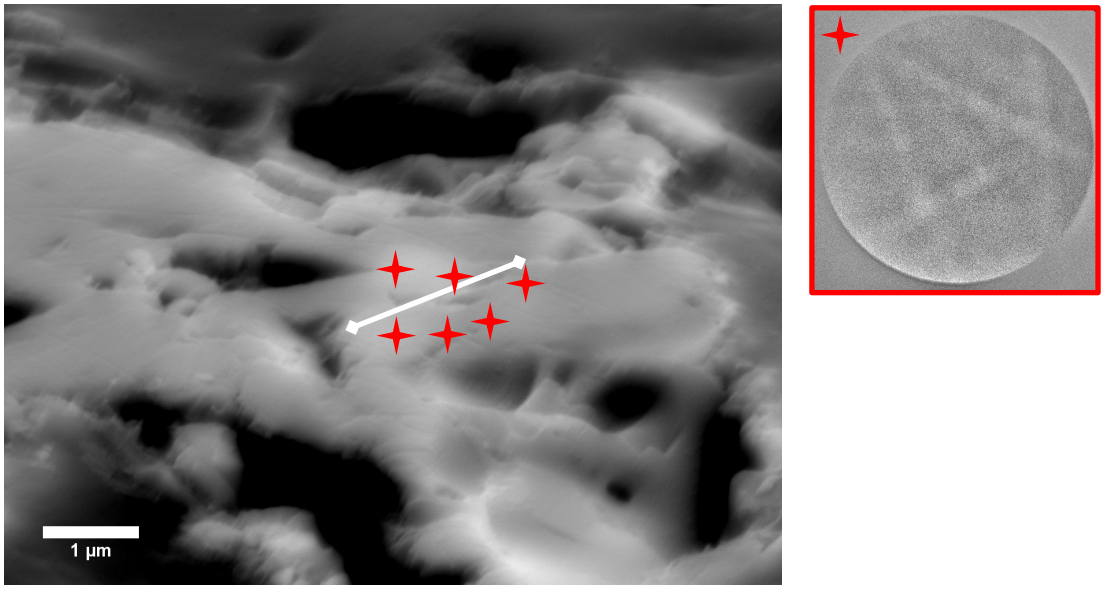

Figure 24: Tilted image of Figure 23 at 70°. EBSD point analysis is denoted by markers, while approximate needle location is shown by the white line. EBSP image is shown for reference.

IV. SUMMARY AND CONCLUSIONS

Reduced $NiAl_2O_4$ + 2.5 wt. % ZrO_2 was characterized during oxidation using *in-situ* HTXRD, *ex-situ* SEM, *in-situ* HTSEM, and EBSD. It has been demonstrated that *in-situ* high resolution low voltage HTSEM can provide useful information about the mechanisms of surface oxidation/deactivation, especially when coupled with HTXRD. The following issues with the techniques have been addressed:

1. The feasibility of observing surface behavior during deactivation and regeneration of the catalyst by reduction and reoxidation;
2. Surface and bulk microstructural evolution during thermal exposure; and
3. Stability of surface and bulk morphology over time at operating temperatures.

The overall reduction and reoxidation process can be expressed as:

$$NiAl_2O_4 \xrightarrow{H_2+heat} Ni_{1-x}Al_2O_{4-x} + xNi + \frac{x}{2}O_2 \xrightarrow{O_2+heat} xNiO + Ni_{1-x}Al_2O_{4-x} \xrightarrow{time+heat} NiAl_2O_4.$$

Diffraction patterns obtained from the HTXRD experiment in air demonstrate the transition from Ni to NiO begins within the temperature range of 400-500°C and concludes between 800-900°C. Reincorporation of the NiO into the defect spinel occurs at temperatures between 900-1100°C, with residual NiO still present in the pattern taken at room temperature after cooling. No changes in peak positions were observed in patterns collected from the HTXRD experiment in industrial N_2 upon heating until 1100°C where NiO is formed. Upon cooling, small amounts of NiO become apparent, indicating slight oxidation occurred with small traces of oxygen. No secondary phases were present within the patterns collected in air or N_2, nor were transition to higher alumina polymorphs observed.

Characterization of the surface of the reduced composite via SEM show that support surface morphology changes and Ni particle size increases with temperature. Morphology of the support surface alters from a continuous faceted structure to a structure with long traversing crevasses that develop between 750 and 900°C. Reduction below 900°C yields undefined Ni particle shapes, whereas particles exhibit faceting above this temperature as T_R is approached. Shape and size of the Ni particles at temperatures above 900°C is determined by location upon the support, i.e., whether the

Ni particle is positioned on a flat or stepped surface. Cross sectioning of reduced particles reveal Ni needle-like features with either parallel or regularly intersecting orientations indicating the inclusions are crystallographic in nature. In conjunction with the presented EBSD results, it has been proposed that these features form within grains, presumably by short circuit diffusion mechanisms. Highly aligned porosity is also observed throughout the reduced sample bulk. Both needles and porosity are not present upon oxidation suggesting that the bulk is reversible upon oxidation.

In-situ HTSEM performed in high vacuum on a 900°C reduced $NiAl_2O_4$ sample demonstrates that at relevant operation temperatures and pO_2, the Ni surface particles migrate and coalesce between 900 and 1000°C before reincorporation into the defective spinel can occur. Particle migration and coalescence reveal that the underlying surface of the catalyst is roughened and littered by pitting which also occurs upon reincorporation of the Ni in the matrix. Migrating particle composition is not known, but HTXRD in N_2 indicates that these are either Ni, or consist of a Ni core with and oxidized outer shell. Mechanisms for the migration and coalescence under the imaging conditions are unclear; movement is not gravity driven and the Ni is not a liquid. Nanoparticles, roughly 10nm in diameter, emerge from the matrix when 900-1000°C is reached, and appear to be stable. Evolution of these features is a direct result of low pO_2 conditions within the SEM resulting in further reduction of the matrix at this temperature. When 1100°C is reached, all particles reincorporate with the matrix, and matrix damaging and removal is evident by deposition of material which was confirmed with EDS. HTXRD indicates that this is not a temperature induced phase change, although interaction with the electron beam may encourage transformation.

Ex-situ HTSEM was performed on re-oxidized samples which exhibited more defined pitting, from poorly defined geometrical shapes into well-defined squares and triangles. Shallow faceting and nanopitting disappear with increased pO_2, presumably to growth of larger features or by mass transport across the surface. The ZrO_2 changes position, but maintains the spherical morphology upon heating, sinking into the spinel. Crater like indentations from Ni particles on the ZrO_2 heal with heat and time. This indicates that the interface between the support and the modifier is rearranging. Pitting from Ni particle migration, coalescence, and recombination did not heal during 1 and 4

hour holds at 1100°C under atmospheric pO_2, indicating that surface roughening does not heal, and that the microstructure matures with time over temperature.

EBSD was performed on the matrix as well as the Ni surface particles, showing that matrix orientations could be inspected visually. No definitive conclusions on particle orientations could be drawn. However, bulk cross section investigation of orientations collected around needle-like features support the hypothesis that the inclusions form within the grain, presumably at crystallographic orientations.

Overall, this work provides direct observation of the deactivation mechanisms of metal supported catalysts along with microstructural changes. The results presented lend insights to understanding these deactivation mechanisms and in turn may lead to tailored supports to prolong catalyst lifetime.

V. FUTURE WORK

More work is needed to fully understand regeneration, maturation of the microstructure, and the effects a roughened surface may have on the effective diffusion rates specifically on particle ability to migrate and coalesce. *In-situ* cycling via HTSEM, specifically observations in a reducing environment and subsequently oxidizing the sample, may prove insightful for these issues. Within the literature, imaging has been performed in a reducing environment, He + 4% H_2. However, our current HTSEM system requires modifications to allow this feature[65, 66]. Therefore, new instrumentation or experimental setup may be required to perform such evaluations at Alfred University.

The use of a reducing atmosphere within the HTSEM system allows for many experiments to be conceived. For example, *in-situ* reduction can be performed, possibly monitoring and characterizing the surface during the initial stages of the reduction process with respect to temperature. Mechanisms for particle size differences according to reduction temperature can be observed as well as microstructural changes upon the surface. *In-situ* cycling is another experiment that could lead to a greater understanding of the regeneration process, especially if the experiments could be correlated with HTXRD. This could allow for observations of the mechanisms that the reduced catalyst undergoes during the deactivation, recombination, and the subsequent reduction processes to fully characterize the regeneration process. Experiments such as this can reinforce the claim of microstructural maturation, and enable comparison of recombination rates of fresh vs. regenerated catalysts. Also, varying reduction temperatures should be explored to evaluate the aforementioned differences in the deactivation and parent phase regeneration.

Other compositions within the $Ni_xMg_{1-x}Al_2O_4$ series should be explored with HTSEM under the conditions used in this study to evaluate the behavior of particle deactivation and reincorporation with respect to composition. Stability of the spinel with respect to composition can also lend insight into matrix degradation, ZrO_2 behavior, and recombination of the NiO particles with the matrix.

Modeling of the matrix damage via Monte Carlo simulations and energy deposition calculations may also be able to prove that the damage caused by the beam is in fact a phase transition. This is inherently difficult due to the low accelerating potential required for observation as well as electron interaction physics (and therefore simulation) below 50 eV in solids, but may be feasible with new methods.

Sinking of the ZrO_2 particles is intriguing, and can be evaluated with a set of simple yet time consuming experiments. Identifying the mass transfer around ZrO_2 by using a monolithic spinel sprinkled with yttria stabilized ZrO_2 (YSZ) which can be heated and compared to our observations. One could identify if the mass transport is universal or if it is specific to our $NiAl_2O_4$ sample via heating the sample with HTSEM or by an *ex-situ* method.

3D morphologies of the Ni needle-like features observed in the cross sections can be confirmed with a combination of FIB and SEM. The orientations of these needles within the matrix are of some interest, and can be obtained by evaluating the orientation of the needle within the matrix. Etching the Ni away using acid is also another possibility, but needs to be performed with some caution. If the structures are 3D in nature, etching away the structures may compromise the mechanical integrity of the spinel particle, causing it to crumble.

EBSD is able to identify particle registry on the support surface and may also lend valuable information of the roughened surface effects. Through this analysis, some conclusions on particle motion and its relation to surface registry could be possible.

REFERENCES

[1] P. Porta, F.S. Stone, and R.G. Turner, "The distribution of nickel ions among octahedral and tetrahedral sites in NiAl2O4-MgAl2O4 solid solutions," *J. Solid State Chem.*, **11** [2] 135–147 (1974).

[2] C.H. Bartholomew, "Sintering kinetics of supported metals: new perspectives from a unifying GPLE treatment," *Appl. Catal. Gen.*, **107** [1] 1–57 (1993).

[3] F. Frusteri, S. Freni, V. Chiodo, L. Spadaro, O. Di Blasi, G. Bonura, and S. Cavallaro, "Steam reforming of bio-ethanol on alkali-doped Ni/MgO catalysts: hydrogen production for MC fuel cell," *Appl. Catal. Gen.*, **270** [1–2] 1–7 (2004).

[4] F. Frusteri, S. Freni, V. Chiodo, S. Donato, G. Bonura, and S. Cavallaro, "Steam and auto-thermal reforming of bio-ethanol over MgO and Ni supported catalysts," *Int. J. Hydrog. Energy*, **31** [15] 2193–2199 (2006).

[5] A.E. Galetti, M.F. Gomez, L.A. Arrúa, and M.C. Abello, "Hydrogen production by ethanol reforming over NiZnAl catalysts: Influence of Ce addition on carbon deposition," *Appl. Catal. Gen.*, **348** [1] 94–102 (2008).

[6] A.E. Galetti, M.F. Gomez, L.A. Arrua, A.J. Marchi, and M.C. Abello, "Study of CuCoZnAl oxide as catalyst for the hydrogen production from ethanol reforming," *Catal. Commun.*, **9** [6] 1201–1208 (2008).

[7] N. Laosiripojana, S. Assabumrungrat, and S. Charojrochkul, "Steam reforming of ethanol with co-fed oxygen and hydrogen over Ni on high surface area ceria support," *Appl. Catal. Gen.*, **327** [2] 180–188 (2007).

[8] J.R. Rostrup-Nielsen, "Sulfur-passivated nickel catalysts for carbon-free steam reforming of methane," *J. Catal.*, **85** [1] 31–43 (1984).

[9] B. Zhang, X. Tang, Y. Li, W. Cai, Y. Xu, and W. Shen, "Steam reforming of bio-ethanol for the production of hydrogen over ceria-supported Co, Ir and Ni catalysts," *Catal. Commun.*, **7** [6] 367–372 (2006).

[10] M.E. Miller and S.T. Misture, "Idealizing γ-Al2O3: In Situ Determination of Nonstoichiometric Spinel Defect Structure," *J. Phys. Chem. C*, **114** [30] 13039–13046 (2010).

[11] B.E. Hill and S.T. Misture, "Atomic Scale Mechanisms of the Reduction of Nickel-Magnesium Aluminate Spinels," *J. Am. Ceram. Soc.*, **96** [11] 3603–3608 (2013).

[12] S.T. Misture, K.M. McDevitt, K.C. Glass, D.D. Edwards, J.Y. Howe, K.D. Rector, H. He, and S.C. Vogel, "Sulfur-resistant and regenerable Ni/Co spinel-based catalysts for methane dry reforming," *Catal. Sci. Technol.*, **5** [9] 4565–4574 (2015).

[13] K. Miyatani, Y. Wada, and F. Okamoto, "Magnetic Properties of Single Crystal Chalcogenide Spinels; CuCr2X3Y (X=S, Se and Te, Y=C1, Br and I) System," *J. Phys. Soc. Jpn.*, **25** [2] 369–372 (1968).

[14] K.E. Sickafus, J.M. Wills, and N.W. Grimes, "Structure of Spinel," *J. Am. Ceram. Soc.*, **82** [12] 3279–3292 (1999).

[15] K. Mocala and A. Navrotsky, "Structural and Thermodynamic Variation in Nickel Aluminate Spinel," *J. Am. Ceram. Soc.*, **72** [5] 826–832 (1989).

[16] I. Halevy, D. Dragoi, E. Üstündag, A.F. Yue, E.H. Arredondo, J. Hu, and M.S. Somayazulu, "The effect of pressure on the structure of NiAl 2 O 4," *J. Phys. Condens. Matter*, **14** [44] 10511 (2002).

[17] H.S.C. O'Neill and A. Navrotsky, "Simple spinels; crystallographic parameters, cation radii, lattice energies, and cation distribution," *Am. Mineral.*, **68** [1–2] 181–194

(1983).

[18] R.J. Hill, J.R. Craig, and G.V. Gibbs, "Systematics of the spinel structure type," *Phys. Chem. Miner.*, **4** [4] 317–339 (1979).

[19] N.W. Grimes, "The spinels: versatile materials," *Phys. Technol.*, **6** [1] 22 (1975).

[20] J.A. Ball, S.T. Murphy, R.W. Grimes, D. Bacorisen, R. Smith, B.P. Uberuaga, and K.E. Sickafus, "Defect processes in MgAl2O4 spinel," *Solid State Sci.*, **10** [6] 717–724 (2008).

[21] I.E. Achouri, N. Abatzoglou, C. Fauteux-Lefebvre, and N. Braidy, "Diesel steam reforming: Comparison of two nickel aluminate catalysts prepared by wet-impregnation and co-precipitation," *Catal. Today*, **207** 13–20 (2013).

[22] C. Fauteux-Lefebvre, N. Abatzoglou, N. Braidy, and I.E. Achouri, "Diesel steam reforming with a nickel–alumina spinel catalyst for solid oxide fuel cell application," *J. Power Sources*, **196** [18] 7673–7680 (2011).

[23] Y. Cesteros, P. Salagre, F. Medina, and J.E. Sueiras, "Synthesis and characterization of several Ni/NiAl2O4 catalysts active for the 1,2,4-trichlorobenzene hydrodechlorination," *Appl. Catal. B Environ.*, **25** [4] 213–227 (2000).

[24] H. Muroyama, R. Nakase, T. Matsui, and K. Eguchi, "Ethanol steam reforming over Ni-based spinel oxide," *Int. J. Hydrog. Energy*, **35** [4] 1575–1581 (2010).

[25] N. Sahli, C. Petit, A.C. Roger, A. Kiennemann, S. Libs, and M.M. Bettahar, "Ni catalysts from NiAl2O4 spinel for CO2 reforming of methane," *Catal. Today*, **113** [3–4] 187–193 (2006).

[26] K.V.R. Chary, P.V. Ramana Rao, and V. Venkat Rao, "Catalytic functionalities of nickel supported on different polymorphs of alumina," *Catal. Commun.*, **9** [5] 886–

893 (2008).

[27] M. Miller, “Nanoporous glass-ceramics for gas separation;” Ph.D. Thesis, Alfred University, Alfred, NY, 2008.

[28] B. Hill, “Characterizing the Reduction of NixMg1-xAl2O4;” Ph.D. Thesis, Alfred University, Alfred, NY, 2012.

[29] Y. Okuyama, N. Kurita, and N. Fukatsu, “Defect structure of alumina-rich nonstoichiometric magnesium aluminate spinel,” *Solid State Ion.*, **177** [1–2] 59–64 (2006).

[30] O. Quénard, C. Laurent, M. Brieu, and A. Rousset, “Synthesis, microstructure and oxidation of Co-MgAl2O4 and Ni-MgAl2O4 nanocomposite powders,” *Nanostructured Mater.*, **7** [5] 497–507 (1996).

[31] M.E. Miller and S.T. Misture, “Stoichiometric (Ni,Mg)-Cordierite Glass–Ceramics,” *J. Am. Ceram. Soc.*, **93** [4] 1018–1025 (2010).

[32] F.A. Elrefaie and W.W. Smeltzer, “Thermodynamics of Nickel-Aluminum-Oxygen System Between 900 and 1400 K,” *J. Electrochem. Soc.*, **128** [10] 2237–2242 (1981).

[33] H. Kishimoto, K. Yamaji, M.E. Brito, T. Horita, and H. Yokokawa, “Generalized Ellingham diagrams for utilization in solid oxide fuel cells,” *J. Min. Metall. Sect. B Metall.*, **44** [1] 39–48 (2008).

[34] J.R. Taylor and A.T. Dinsdale, “A thermodynamic assessment of the Ni-O, Cr-O and Cr-Ni-O systems using the ionic liquid and compound energy models,” *Z. Für Met.*, **81** [5] 354–366 (1990).

[35] J. Mermelstein, N. Brandon, and M. Millan, “Impact of Steam on the Interaction between Biomass Gasification Tars and Nickel-Based Solid Oxide Fuel Cell Anode

Materials," *Energy Fuels*, **23** [10] 5042–5048 (2009).

[36] M. Kowalski and P.J. Spencer, "Thermodynamic reevaluation of the C-O, Fe-O and Ni-O systems: Remodelling of the liquid, BCC and FCC phases," *Calphad*, **19** [3] 229–243 (1995).

[37] I. Levin and D. Brandon, "Metastable alumina polymorphs : Crystal structures and transition sequences," *J. Am. Ceram. Soc.*, **81** [8] 1995–2012 (1998).

[38] K. Wefers and C. Misra, "Oxides and Hydroxides of Aluminum," *Alcoa Tech. Pap. No 19 Revis.*, 75 (1987).

[39] E. Üstündag, P. Ret, R. Subramanian, R. Dieckmann, and S.L. Sass, "In situ metal-ceramic microstructures by partial reduction reactions in the Ni-Al-O system and the role of ZrO2," *Mater. Sci. Eng. A*, **195** 39–50 (1995).

[40] S.J. Han, Y. Bang, J.G. Seo, J. Yoo, and I.K. Song, "Hydrogen production by steam reforming of ethanol over mesoporous Ni–Al2O3–ZrO2 xerogel catalysts: Effect of Zr/Al molar ratio," *Int. J. Hydrog. Energy*, **38** [3] 1376–1383 (2013).

[41] M. Boudart, "Turnover Rates in Heterogeneous Catalysis," *Chem. Rev.*, **95** [3] 661–666 (1995).

[42] F. Pompeo, N.N. Nichio, M.M.V.M. Souza, D.V. Cesar, O.A. Ferretti, and M. Schmal, "Study of Ni and Pt catalysts supported on α-Al2O3 and ZrO2 applied in methane reforming with CO2," *Appl. Catal. Gen.*, **316** [2] 175–183 (2007).

[43] S.P. Chen, D.J. Srolovitz, and A.F. Voter, "Computer simulation on surfaces and [001] symmetric tilt grain boundaries in Ni, Al, and Ni3Al," *J. Mater. Res.*, **4** [1] 62–77 (1989).

[44] S.M. Foiles, M.I. Baskes, and M.S. Daw, "Embedded-atom-method functions for the

fcc metals Cu, Ag, Au, Ni, Pd, Pt, and their alloys," *Phys. Rev. B*, **33** [12] 7983–7991 (1986).

[45] R.A. Johnson, "Analytic nearest-neighbor model for fcc metals," *Phys. Rev. B*, **37** [8] 3924–3931 (1988).

[46] V.M. Kuznetsov, R.I. Kadyrov, and G.E. Rudenskii, "Calculation of Surface Energy of Metals and Alloys by the Electron Density Functional Method," *J. Mater. Sci. Technol.*, **14** 320–322 (1998).

[47] H. Meltzman, D. Chatain, D. Avizemer, T.M. Besmann, and W.D. Kaplan, "The equilibrium crystal shape of nickel," *Acta Mater.*, **59** [9] 3473–3483 (2011).

[48] Y.-N. Wen and J.-M. Zhang, "Surface energy calculation of the fcc metals by using the MAEAM," *Solid State Commun.*, **144** [3–4] 163–167 (2007).

[49] K.A. Rogers and K.P. Trumble, "Effect of reduction temperature on internal reduction microstructures," *Scr. Mater.*, **39** [1] 103–108 (1998).

[50] Y. Guo, L. Zhou, and H. Kameyama, "Steam reforming reactions over a metal-monolithic anodic alumina-supported Ni catalyst with trace amounts of noble metal," *Int. J. Hydrog. Energy*, **36** [9] 5321–5333 (2011).

[51] S.M. Hashhemnjad and M. Parvari, "Deactivation and Regeneration of Nickel-Based Catalysts for Steam-Methane Reforming," *Chin. J. Catal.*, **32** [1–2] 273–279 (2011).

[52] D. Li, I. Atake, T. Shishido, Y. Oumi, T. Sano, and K. Takehira, "Self-regenerative activity of Ni/Mg(Al)O catalysts with trace Ru during daily start-up and shut-down operation of CH4 steam reforming," *J. Catal.*, **250** [2] 299–312 (2007).

[53] D. Li, T. Shishido, Y. Oumi, T. Sano, and K. Takehira, "Self-activation and self-regenerative activity of trace Rh-doped Ni/Mg(Al)O catalysts in steam reforming of

methane," *Appl. Catal. Gen.*, **332** [1] 98–109 (2007).

[54] J.R. Rostrup-Nielsen, "Some principles relating to the regeneration of sulfur-poisoned nickel catalyst," *J. Catal.*, **21** [2] 171–178 (1971).

[55] H. Tanaka, M. Uenishi, M. Taniguchi, I. Tan, K. Narita, M. Kimura, K. Kaneko, Y. Nishihata, *et al.*, "The intelligent catalyst having the self-regenerative function of Pd, Rh and Pt for automotive emissions control," *Catal. Today*, **117** [1–3] 321–328 (2006).

[56] L.G. Felix, D.M. Rue, T.P.S. III, and L.E. Weast, "Method for producing catalytically active glass-ceramic materials, and glass-ceramics produced thereby," U.S. Pat. 20090011925 A1, 2009.

[57] L.G. Felix, C.W. Choi, D.M. Rue, L.E. Weast, and T.P. Seward, "Robust glass-ceramics catalysts for biomass gasification," *Environ. Prog. Sustain. Energy*, **28** [3] 336–346 (2009).

[58] J.N. Kuhn, Z. Zhao, A. Senefeld-Naber, L.G. Felix, R.B. Slimane, C.W. Choi, and U.S. Ozkan, "Ni-olivine catalysts prepared by thermal impregnation: Structure, steam reforming activity, and stability," *Appl. Catal. Gen.*, **341** [1–2] 43–49 (2008).

[59] Z. Zhao, N. Lakshminarayanan, J.N. Kuhn, A. Senefeld-Naber, L.G. Felix, R.B. Slimane, C.W. Choi, and U.S. Ozkan, "Optimization of thermally impregnated Ni–olivine catalysts for tar removal," *Appl. Catal. Gen.*, **363** [1–2] 64–72 (2009).

[60] Z. Zhao, J.N. Kuhn, L.G. Felix, R.B. Slimane, C.W. Choi, and U.S. Ozkan, "Thermally Impregnated Ni−Olivine Catalysts for Tar Removal by Steam Reforming in Biomass Gasifiers," *Ind. Eng. Chem. Res.*, **47** [3] 717–723 (2008).

[61] T.A. Hardt and R.W. Knowles, "High temperature specimen stage and detector for an

environmental scanning electron microscope," E.P. 1003200 A1, 2000.

[62] D.R. Sample, P.W. Brown, and J.P. Dougherty, "Microstructural Evolution of Copper Thick Films Observed by Environmental Scanning Electron Microscopy," *J. Am. Ceram. Soc.*, **79** [5] 1303–1306 (1996).

[63] B.A. Wilson and E.D. Case, "In situ microscopy of crack healing in borosilicate glass," *J. Mater. Sci.*, **32** [12] 3163–3175 (1997).

[64] R. Podor, J. Ravaux, and H.-P. Brau, "In Situ Experiments in the Scanning Electron Microscope Chamber;" in Scanning Electron Microscopy. 2012.

[65] T. Klemensø, C.C. Appel, and M. Mogensen, "In Situ Observations of Microstructural Changes in SOFC Anodes during Redox Cycling," *Electrochem. Solid-State Lett.*, **9** [9] A403–A407 (2006).

[66] Y. Nakagawa, K. Yashiro, K. Sato, T. Kawada, and J. Mizusaki, "Microstructural Changes of Ni/YSZ Cermet under Repeated Redox Reaction in Environmental Scanning Electron Microscope (ESEM)," *ECS Trans.*, **7** [1] 1373–1380 (2007).

[67] Protochips, "EDS in the TEM and SEM using Aduro," *Protochips Inc Appl. Note*, [AA] 5.3 (2015).

[68] Protochips, "Correlative Analysis in the TEM and SEM Kirkendall Effect Zinc Oxide/Alumina Spinel Formation Observed In Situ," *Protochips Inc Appl. Note*, [AA] 1.3 (2015).

[69] Protochips, "Sample Preparation Guide Preparing Particles on Aduro E-Chips," *Protochips Inc Appl. Note*, (2015).

[70] H.S.C. O'Neill, W.A. Dollase, and C.R.R. Ii, "Temperature dependence of the cation distribution in nickel aluminate (NiAl2O4) spinel: a powder XRD study," *Phys.*

Chem. Miner., **18** [5] 302–319 (1991).

[71] C. Bale, *F.A.C.T. (Facility for the Analysis of Chemical Thermodynamics)*. Thermfact and GTT-Technologies, 2016.

[72] S.M. Lakiza and L.M. Lopato, "Stable and Metastable Phase Relations in the System Alumina–Zirconia–Yttria," *J. Am. Ceram. Soc.*, **80** [4] 893–902 (1997).

[73] B. Phillips, J.J. Hutta, and I. Warshaw, "Phase Equilibria in the System NiO–Al2O3–SiO2," *J. Am. Ceram. Soc.*, **46** [12] 579–583 (1963).

[74] T.W. Hansen, A.T. Delariva, S.R. Challa, and A.K. Datye, "Sintering of catalytic nanoparticles: particle migration or Ostwald ripening?," *Acc. Chem. Res.*, **46** [8] 1720–1730 (2013).

[75] J. Sehested, "Sintering of nickel steam-reforming catalysts," *J. Catal.*, **217** [2] 417–426 (2003).

[76] P. Wynblatt and N.A. Gjostein, "Supported metal crystallites," *Prog. Solid State Chem.*, **9** 21–58 (1975).

[77] E. Ruckenstein and S.H. Lee, "Redispersion and migration of Ni supported on alumina," *J. Catal.*, **86** [2] 457–464 (1984).

[78] E. Ruckenstein and Y.F. Chu, "Redispersion of platinum crystallites supported on alumina—Role of wetting," *J. Catal.*, **59** [1] 109–122 (1979).

[79] L.P. Bonfrisco and M. Frary, "Effects of crystallographic orientation on the early stages of oxidation in nickel and chromium," *J. Mater. Sci.*, **45** [6] 1663–1671 (2010).

[80] J.V. Cathcart, G.F. Petersen, and C.J. Sparks, "The Structure of Thin Oxide Films Formed on Nickel Crystals," *J. Electrochem. Soc.*, **116** [5] 664–668 (1969).

[81] N.N. Khoi, W.W. Smeltzer, and J.D. Embury, "Growth and Structure of Nickel Oxide

on Nickel Crystal Faces," *J. Electrochem. Soc.*, **122** [11] 1495–1503 (1975).

[82] T.V. Reshetenko, L.B. Avdeeva, Z.R. Ismagilov, and A.L. Chuvilin, "Catalytic filamentous carbon as supports for nickel catalysts," *Carbon*, **42** [1] 143–148 (2004).

[83] B. Bonvalot-Dubois, G. Dhalenne, J. Berthon, A. Revcolevschi, and R. a. Rapp, "Reduction of NiO Platelets in a NiO/ZrO2(CaO) Directional Composite," *J. Am. Ceram. Soc.*, **71** [4] 296–301 (1988).

[84] N. Jiang, "Electron beam damage in oxides: a review," *Rep. Prog. Phys.*, **79** [1] 16501 (2016).

[85] R. Castaing, "Electron Probe Microanalysis;" pp. 317–386 in Advances in Electronics and Electron Physics, Edited by L.M. and C. Marton. Academic Press, 1960.

[86] O. Jbara, S. Fakhfakh, M. Belhaj, S. Rondot, A. Hadjadj, and J.M. Patat, "Charging effects of PET under electron beam irradiation in a SEM," *J. Phys. Appl. Phys.*, **41** [24] 245504 (2008).

[87] D.C. Joy and C.S. Joy, "Low voltage scanning electron microscopy," *Micron*, **27** [3–4] 247–263 (1996).

[88] R.F. Egerton, P. Li, and M. Malac, "Radiation damage in the TEM and SEM," *Micron*, **35** [6] 399–409 (2004).

[89] P. Li and R.F. Egerton, "Radiation damage in coronene, rubrene and p-terphenyl, measured for incident electrons of kinetic energy between 100 and 200 kev," *Ultramicroscopy*, **101** [2–4] 161–172 (2004).

[90] N. Jiang and J.C.H. Spence, "Electronic ionization induced atom migration in spinel MgAl2O4," *J. Nucl. Mater.*, **403** [1–3] 147–151 (2010).

[91] S.P.S. Badwal, "Zirconia-based solid electrolytes: microstructure, stability and ionic

conductivity," *Solid State Ion.*, **52** [1] 23–32 (1992).

[92] U. Brossmann, R. Würschum, and U. Södervall, "Oxygen diffusion in ultrafine grained monoclinic ZrO2," *J. Appl. Phys.*, **85** [11] 7646–7654 (1999).

[93] B.W. Busch, W.H. Schulte, E. Garfunkel, T. Gustafsson, W. Qi, R. Nieh, and J. Lee, "Oxygen exchange and transport in thin zirconia films on Si(100)," *Phys. Rev. B*, **62** [20] R13290–R13293 (2000).

[94] S. Appari, V.M. Janardhanan, R. Bauri, and S. Jayanti, "Deactivation and regeneration of Ni catalyst during steam reforming of model biogas: An experimental investigation," *Int. J. Hydrog. Energy*, **39** [1] 297–304 (2014).

[95] L. Li, C. Howard, D.L. King, M. Gerber, R. Dagle, and D. Stevens, "Regeneration of Sulfur Deactivated Ni-Based Biomass Syngas Cleaning Catalysts," *Ind. Eng. Chem. Res.*, **49** [20] 10144–10148 (2010).

[96] EDAX, "ChI-Scan for phase differentiation using combined simultaneously collected EDS and EBSD data," *EDAX Appl. Note - EBSD*, (2012).

[97] Oxford Instruments, "AZtec Tru-I The Most Accurate EBSD Results," *Oxf. Instrum. Plc Appl. Note*, (2015).

[98] K.Z. Baba-Kishi, "Review Electron backscatter Kikuchi diffraction in the scanning electron microscope for crystallographic analysis," *J. Mater. Sci.*, **37** [9] 1715–1746 (2002).

[99] W. Wisniewski, M. Nagel, G. Völksch, and C. Rüssel, "New Insights into the Microstructure of Oriented Fresnoite Dendrites in the System Ba2TiSi2O8−SiO2 Through Electron Backscatter Diffraction (EBSD)," *Cryst. Growth Des.*, **10** [4] 1939–1945 (2010).

APPENDIX 1 – PYTHON CODE

A. Video Editing

```
# -*- coding: utf-8 -*-
"""
Created on Mon Apr 27 15:30:19 2015

@author: paytone
@revised by aladonis
"""

from moviepy.editor import *
import numpy as np
from moviepy.tools import cvsecs

'Import videos as variables; example: directory/filename.filetype'
vidloc1 = 'D:\Ni cataysts work\Ni1Zr videos\High Vacuum High Mag/NI1Zr first part.avi'
vidloc2 = 'D:\Ni cataysts work\Ni1Zr videos\High Vacuum High Mag/NI1Zr second part.avi'
vidloc3 = 'F:\Python Code for Video\Ni cataysts work\Ni1Zr videos\High Vacuum Low
Mag/NI1Zr third part low mag.avi'
vidloc4 = 'F:\Python Code for Video\Ni cataysts work\Ni1Zr videos\High Vacuum Low
Mag/NI1Zr fourth part low mag.avi'

convertvidloc1 = 'F:\Python Code for Video\Ni cataysts work\Ni1Zr videos\High Vacuum Low
Mag/vidloc1.mp4'
convertvidloc2 = 'F:\Python Code for Video\Ni cataysts work\Ni1Zr videos\High Vacuum Low
Mag/vidloc2.mp4'
convertvidloc3 = 'F:\Python Code for Video\Ni cataysts work\Ni1Zr videos\High Vacuum Low
Mag/vidloc3.mp4'
convertvidloc4 = 'F:\Python Code for Video\Ni cataysts work\Ni1Zr videos\High Vacuum Low
Mag/vidloc4.mp4'

'convert clips into .mp4 files'
clip1 = VideoFileClip(vidloc1)
clip1.write_videofile("vidloc1.mp4", fps=24, bitrate='800k', codec='libx264',
audio=False)
clip2 = VideoFileClip(vidloc2)
clip2.write_videofile("vidloc2.mp4", fps=24, bitrate='800k', codec='libx264',
audio=False)
clip3 = VideoFileClip(vidloc3)
clip3.write_videofile("vidloc3.mp4", fps=24, bitrate='800k', codec='libx264',
audio=False)
clip4 = VideoFileClip(vidloc4)
clip4.write_videofile("vidloc4.mp4", fps=24, bitrate='800k', codec='libx264',
audio=False)


''' Separate video into usable clips for merging or rearranging, .subclip allows to edit
the section of the video. '''
clip1 = VideoFileClip(vidloc1)
#.subclip(0.0, 72.0)
clip2 = VideoFileClip(vidloc2)
#.subclip(0.0, 90.2)
clip3 = VideoFileClip(convertvidloc3)
#.subclip(0.0, 90.2)
clip4 = VideoFileClip(convertvidloc4)
#.subclip(0.0, 90.2)

'freeze last frame of video to account for temp profile'
tfreeze1 = cvsecs((10, 9)) #213s
tfreeze2 = cvsecs((2, 22)) #142s
tfreeze3 = cvsecs((2, 23)) #143s

imfreeze1 = clip1.to_ImageClip(tfreeze1)
imfreeze2 = clip2.to_ImageClip(tfreeze2)
imfreeze3 = clip3.to_ImageClip(tfreeze3)
```

```
clip1freeze = concatenate_videoclips([clip1,
imfreeze1.set_duration(4.263399693721286370597243491577 3)]) #duration is
(realtimepaused*videotime/wholerealvideotime)85*213/1570
clip2freeze = concatenate_videoclips([clip2, imfreeze2.set_duration(4.266666666666667)])
#duration is (realtimepaused*videotime/wholerealvideotime)32*142/1065
clip3freeze = concatenate_videoclips([clip3, imfreeze3.set_duration(4.664490278285182)])
#duration is (realtimepaused*videotime/wholerealvideotime)35*143/1073

''' Move clips together creating a compiled video file, then write to file'''

clipcat = CompositeVideoClip([clip1freeze.set_start(0),

clip2.set_start(tfreeze1+4.263399693721286370597243491577 3)])'

clip3freeze.set_start(213+11.53184713375796+142+4.266666666666667),

clip4.set_start(213+11.53184713375796+142+4.266666666666667+143+4.664490278285182)])

clipcat.write_videofile("testcat.mp4", fps=24, bitrate='800k', codec='libx264',
audio=False)
```

B. Video Overlay Generation

```
# -*- coding: raw-unicode-escape -*-
"""
Created on Tue Apr 28 11:12:34 2015

@author: paytone
@revised by aladonis
"""

writefilename1 = 'textoverlay.mp4'
writefilename2 = 'testoverlayvideofinalpart1.mp4'
vidloc = 'D:\Ni cataysts work\Ni1Zr videos\High Vacuum High Mag/testcat.mp4'


from moviepy.editor import *
import numpy as np
import datetime as dt
from moviepy.video.fx.crop import crop
import matplotlib.pyplot as plt
from moviepy.tools import cvsecs

vidloc = 'D:\Ni cataysts work\Ni1Zr videos\High Vacuum High Mag/testcat.mp4'
datloc = 'D:\Ni cataysts work\Ni1Zr videos\High Vacuum High
Mag/Aduro_2015_06_08_09_59_28.csv'


# Import a video clip in order to get the frame size in pixels
clip1 = VideoFileClip(vidloc)#.subclip(90.2, (2,12.0))
shp = clip1.get_frame(0).shape[0:2]

playback_framerate = 7651.0/1016.0 # movie duration real time/ movie time. Corruption
error seems to have compressed video by additional factor of 1.533 to our best
calculation.

my_data = np.genfromtxt(datloc, delimiter=',')[1:]
#loc = my_data[1:,2]-my_data[0:-1,2] != 0
#reduced data = my data[loc,:]


'''Create the initial text'''
timestring = 't = {:.1f}'.format(0.0) + ' s'
tempstring = 'T = {:.1f} '.format(my_data[0,2]) + u'\xb0' + 'C'
textstring = timestring + ',  ' + tempstring
print(textstring)

# Generate a text clip. You can customize the font, color, etc.
```

```
txt_clip = TextClip(textstring.encode('raw-unicode-escape'),fontsize=30,color='white',
align='SouthWest', method='caption', size=[shp[1], shp[0]])
# The duration needs to be set at the actual duration divided by the capture framerate
#txt clip = txt clip.set duration(duration / playback framerate)

shift = 0.0 # this is the time between the start of the video and the start of the hot
stage experiment, in seconds
last_time =1016 - shift # to increase the duration of the first text frame written
timestep_limit = 3.0 # prevents too many frames from being created
#curtime = start datetime
curtime = 0.0 + shift
txt_cat = []
for line in my_data:

    duration = (line[0] - last_time)/1000.0 # convert from ms to s
    if duration > timestep_limit:
        # Here we set the duration in the video associated with the last text clip
produced
        txt_clip = txt_clip.set_duration(duration / playback_framerate)
        txt_cat.append(txt_clip)

        # Create new text clip
        curtime += duration #dt.timedelta(seconds=duration)
        #timestring = curtime.strftime('%H:%M:%S')
        timestring = 't = {:.1f}'.format(curtime) + ' s'
        tempstring = 'T = {:.1f} '.format(line[2]) + u'\xb0' + 'C'
        textstring = timestring + ',   ' + tempstring
        print(textstring)

        # Generate a text clip. You can customize the font, color, etc.
        txt_clip = TextClip(textstring.encode('raw-unicode-
escape'),fontsize=30,color='white', align='SouthWest', method='caption', size=[shp[1],
shp[0]])
        # The duration needs to be set at the actual duration divided by the capture
framerate

        last_time = line[0]
txt_clip = txt_clip.set_duration(duration / playback_framerate)
txt_cat.append(txt_clip)
curtime += duration

# Create a final text clip
timestring = 't = {:.1f}'.format(my_data[-1,0]/1000.0) + ' s'
tempstring = 'T = {:.1f} '.format(my_data[-  1,2]) + u'\xb0' + 'C'
textstring = timestring + ',   ' + tempstring
txt_clip = TextClip(textstring.encode('raw-unicode-escape'),fontsize=30,color='white',
align='SouthWest', method='caption', size=[shp[1], shp[0]])
txt_clip = txt_clip.set_duration(np.amax([0.0, 1016.0 - curtime/playback_framerate]))
txt_cat.append(txt_clip)

txt_overlay = concatenate_videoclips(txt_cat, method = "compose")
txt_overlay.write_videofile(writefilename1, fps=24, bitrate='800k', codec='libx264',
audio=False)

# 2053883 / 1000 / 60 = 34.2 minutes
# start time stamp SEM: 14:19:43; End: 14:41:37 = 21.9 minutes
# original corrupt video is 3:25, fixed video is 2:12. This makes the full video 33.945.

'''
'''

'''Import the clips'''
clip1 = VideoFileClip(vidloc)
clip2 = VideoFileClip(writefilename1)#.subclip(0,2)

''' Initialize the mask'''
x = np.shape(clip1.get_frame(2))
mask = np.ones([x[0], x[1]])

''' Create the mask regions'''
mask[-40:, 0:500] = 0
```

```
mask[-40:, 0:500] = 0 # create a space for the temperature and experiment duration
readout
mask[900:950, 650:800] = 0 # cover up the magnification

''' Verify the mask shape and create imageclip'''
plt.figure
plt.imshow(mask)
textmask = ImageClip(mask, ismask=True)
im = clip1.get_frame(5)[:,:,1]
plt.imshow(im * (1-mask))

''' Create composite video '''
#cmpvid = CompositeVideoClip([clip1, clip2, clip1.set_mask(textmask)])
#final = crop(cmpvid, y1=24) # Crop out the top of the frame containing the instrument
controls
#final.write videofile(writefilename2,fps=24, bitrate='800k', codec='libx264',
audio=False)
```

C. Video and Overlay Combination

```
# -*- coding: utf-8 -*-
"""
Created on Tue Apr 28 13:47:12 2015

@author: paytone
@revised by aladonis
"""
from moviepy.editor import *
from moviepy.video.fx.crop import crop
import numpy as np
import matplotlib.pyplot as plt

vidloc = 'D:\Ni cataysts work\Ni1Zr videos\High Vacuum High Mag/testcat.mp4'
txtloc = 'D:\Ni cataysts work\Ni1Zr videos\High Vacuum High Mag/textoverlay1sthalf.mp4'

'''Import the clips'''
clip1 = VideoFileClip(vidloc)
clip2 = VideoFileClip(txtloc)#.subclip(0,2)

''' Initialize the mask'''
x = np.shape(clip1.get_frame(2))
mask1 = np.ones([x[0], x[1]])
mask2 = np.ones([x[0], x[1]])

''' Create the mask regions'''
mask1[-40:, 0:500] = 0 # create a space for the temperature and experiment duration
readout
mask1[930:952, 650:800] = 0 # cover up the magnification

mask2[-48:, 0:500] = 0 # create a space for the temperature and experiment duration
readout
mask2[900:950, 650:800] = 0 # cover up the magnification

''' Verify the mask shape and create imageclip'''
plt.figure
plt.imshow(mask)
textmask1 = ImageClip(mask1, ismask=True)
textmask2 = ImageClip(mask2, ismask=True)
#im = clip1.get frame(5)[:,:,1]
#plt.imshow(im * (1-mask))

''' Create composite video '''
cmpvid = CompositeVideoClip([clip1, clip2, clip1.set_mask(textmask1),
clip2.set_mask(textmask2)])
final = crop(cmpvid, y1=24) # Crop out the top of the frame containing the instrument
controls
final.write_videofile('Ni1Zr HVHM Final Video 2.mp4',fps=24, bitrate='800k',
codec='libx264', audio=False)
```

APPENDIX 2 – PHASE DIAGRAMS

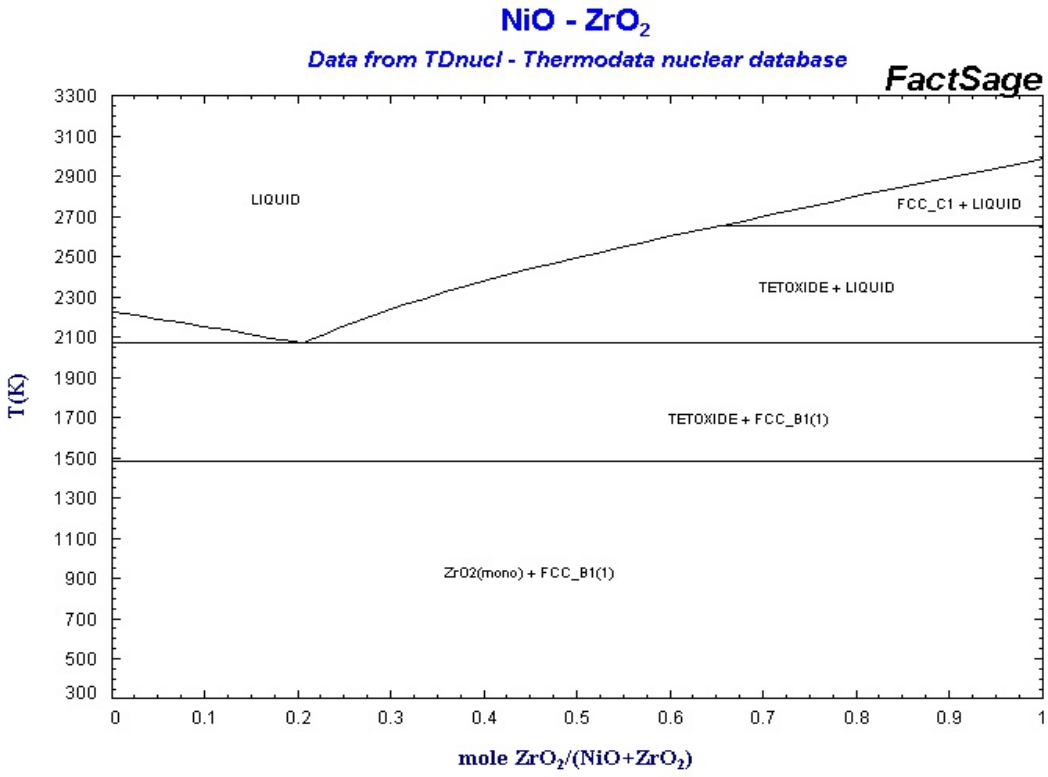

Figure 25: Binary Phase diagram of NiO-ZrO_2 system. [71]

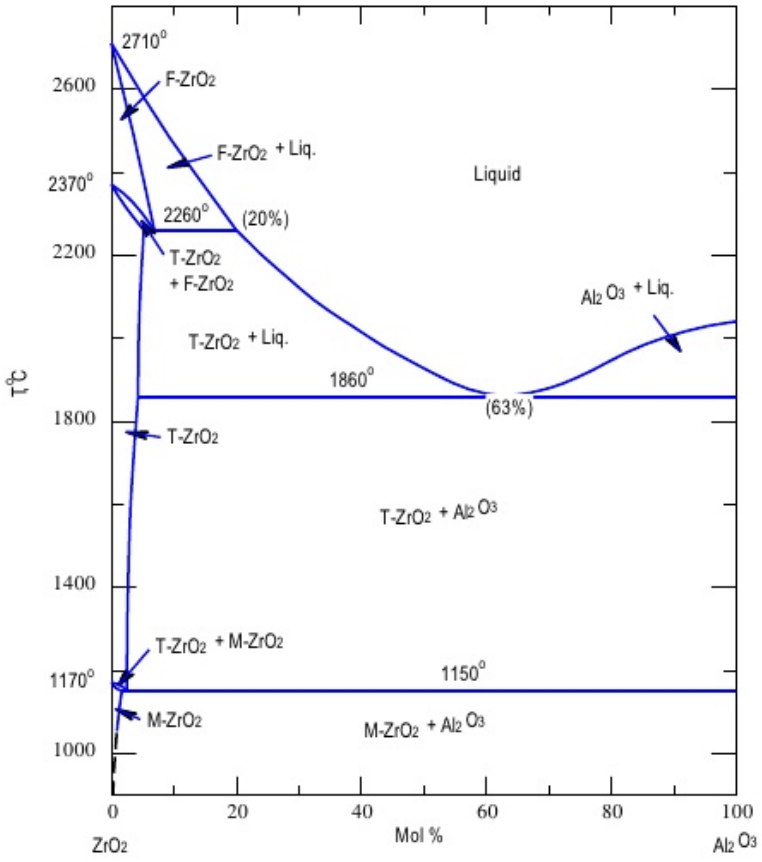

Figure 26: Phase diagram of ZrO_2-Al_2O_3 system. [71, 72]

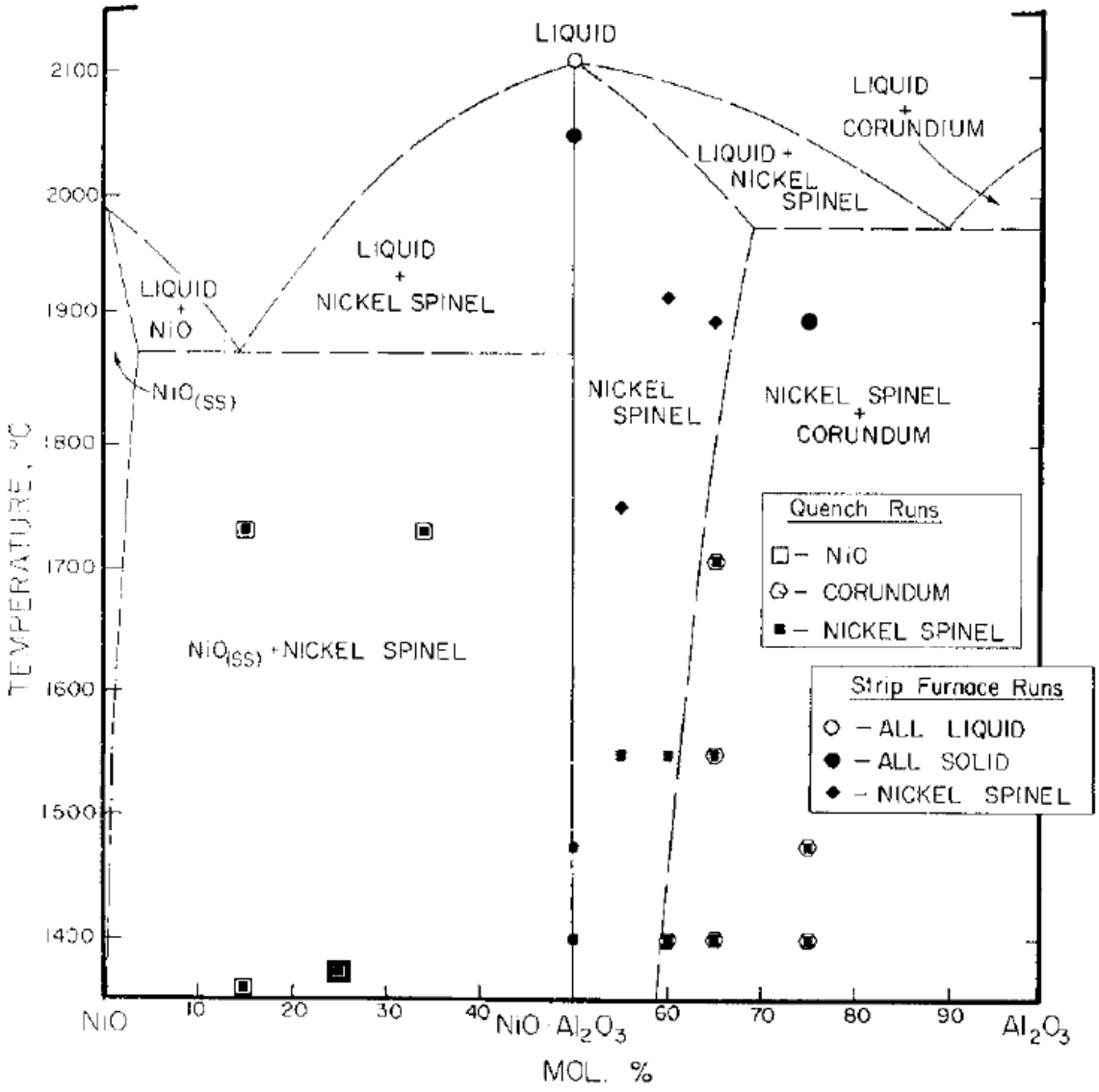

Figure 27: NiO – Al_2O_3 phase diagram.[73]

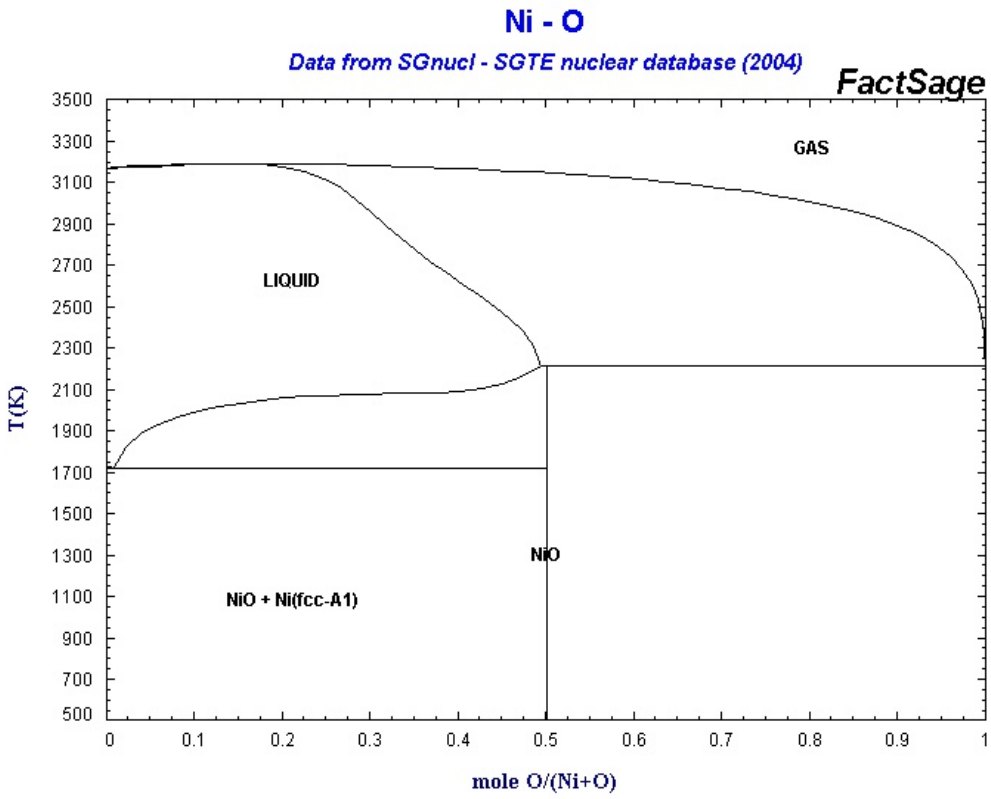

Figure 28: Ni-O system binary phase diagram. [71]